Volume 4 • Number 3 • July 2010
ISSN: 1557-7244

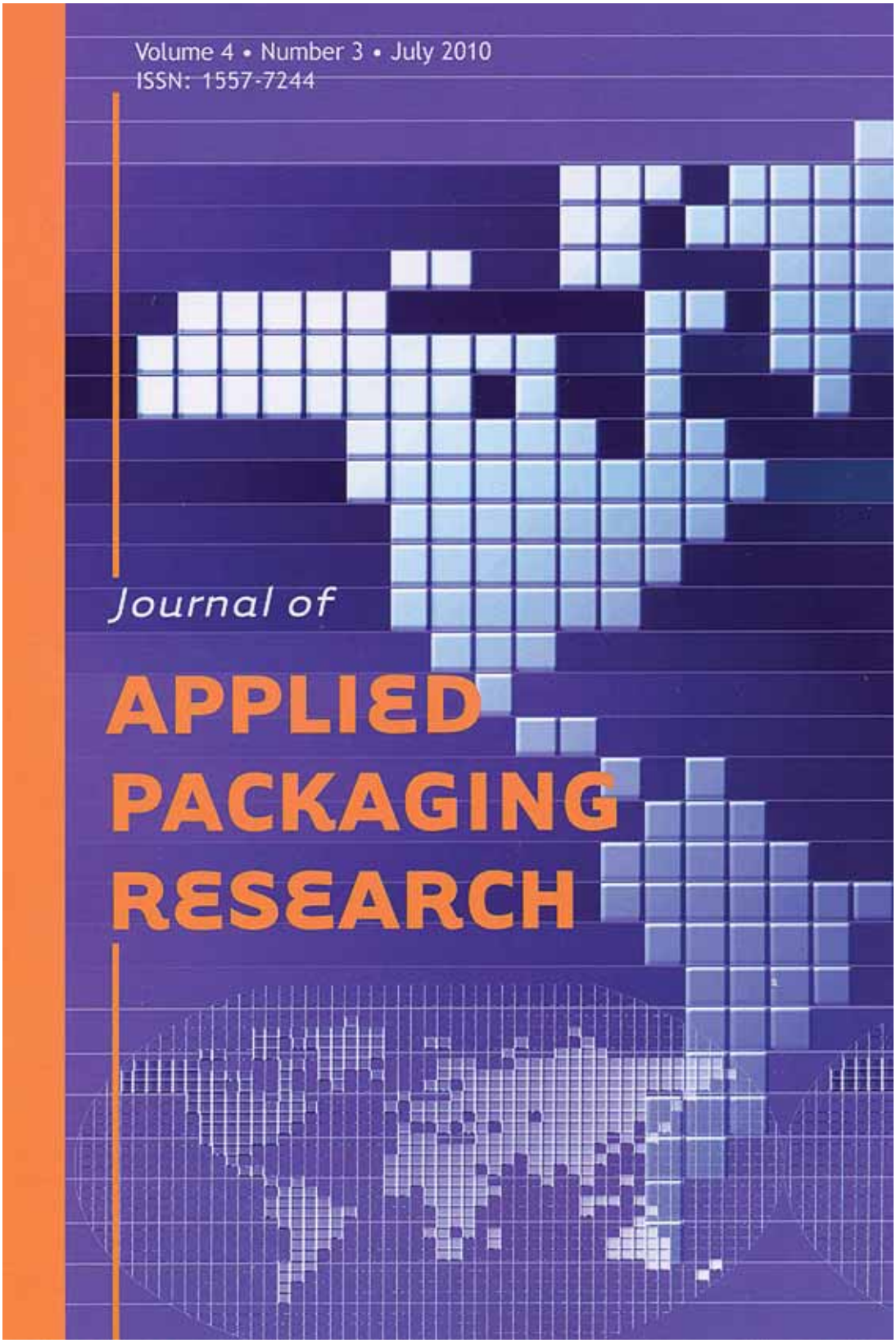

Journal of APPLIED PACKAGING RESEARCH

Aim and Scope

The *Journal of Applied Packaging Research* is an international forum for the dissemination of research papers, review articles, tutorials and news about innovative or emerging technologies for the packaging industry. The journal is targeted towards the broad packaging community including packaging scientists and engineers in industry or academic research and development, food scientists and technologists, materials scientists, mechanical engineers, industrial and systems engineers, toxicologists, analytical chemists, environmental scientists, regulatory officers, and other professionals who are concerned with advances in the development and applications of packaging.

JOURNAL OF APPLIED PACKAGING RESEARCH—Published quarterly—January, April, July and October by DEStech Publications, Inc., 439 North Duke Street, Lancaster, PA 17602-4967.

This journal is recommended by The National Institute of Packaging Handling and Logistics Engineers (www.niphle.org).

Indexed by Chemical Abstracts Service.

Indexed and abstracted by Pira International.

Subscriptions: Annual $319 (Print), $319 (Electronic) and $344 (Print and Electronic). Single copy price $95.00. Foreign subscriptions add $45 per year for postage.

(ISSN 1557-7244)

DEStech Publications, Inc.
439 North Duke Street, Lancaster, PA 17602-4967, U.S.A.

CONTENTS

Research

RESEARCH

Passive UHF RFID Tag Read Performance with Common Packaging Metals

J. SINGH[1,*], J. DANES[2] and M. BROWN[1]
[1]*Industrial Technology, Cal Poly State University, San Luis Obispo, CA 93407*
[2]*Orfalea College of Business, Cal Poly State University, San Luis Obispo, CA 93407*

ABSTRACT: Given a lot of optimistic promise, less than perfect read reliability ranks high on the list of issues related to RFID technology's application in the modern supply chain. This issue is more pronounced when passive UHF tags operate in conjunction with challenging environments such as those that are categorized as detuning or dielectric in nature. Metals fall in the former category and provide a challenging environment as related to 100% data transfer between the UHF tags and the readers. The use of metals such as steel and aluminum is prevalent in packaging applications in the forms of cans, drums, foil and tubes. This study evaluated the performance of five passive UHF tags, advertised to work well under harsh environments, in conjunction with five common applications of metals in packaging i.e. aluminum and steel cans, aseptic carton, flexible snack bag and metal-in static shielding bag. Three dimensional read field mapping was conducted, with over 8775 observations, as per ASTM D7435 to determine readability due to variables such as tag and packaging types, reader antenna attenuation, and the presence or absence of a spacer. Tags dedicated to use with metals performed better than those that were not and a spacer applied between tags and packages generally enhanced the read field. It was also observed that attenuating the reader may provide noticeable improvements in readability for some applications.

1.0 INTRODUCTION

OVER the past decade, radio frequency identification (RFID) has evolved as an automatic identification technology that promises to improve the modern supply chains. With its advantages such as item level tracking, large data capacity, etc. and the promise to reduce labor levels, enhance visibility and improve inventory management, this

*Author to whom correspondence should be addressed. Email: jasingh@calpoly.edu

1557-7244/10/03 115-15

technology is poised to revolutionize supply chain management [1]. RFID, however at its present stage of evolution, is fraught with several issues such as insufficient global standardization, cost, privacy concerns and most importantly - less than perfect read reliability [1]. RFID technology is subject to electrical, reflection, attenuation, scattering and diffraction related interferences that prohibit consistent 100% readability [2].

Several past studies have evaluated the performance of ultra high frequency (UHF) RFID tags and readers in challenging environments such as near those that cause detuning (metals) or are considered high dielectric materials (water). The antenna designs for UHF tags are commonly based on dipole designs compared to multiple loop designs for low frequency (LF) and high frequency (HF). The typical short dipole antennas, with relatively narrow bandwidths, suffer from the problem of fractional bandwidth, which is defined as bandwidth of a device divided by its center frequency [3].

The effective gain of the RFID tag antenna, defined as the ratio of the power required at the input of a loss-free reference antenna to the power supplied to the input of the given antenna to produce, in a given direction, the same field strength at the same distance can be described by the equation $G_{eff} = D\eta\tau$ [4]. Where, D is the directivity of the antenna, η is the antenna efficiency and τ represents power transfer efficiency. When placed next to metal, the directivity tends to increase, efficiency decreases from reduced radiating resistance and the antenna impedance can change significantly thereby causing poor power transfer efficiency. In the vicinity of high dielectric materials such as water, the directivity increases and the efficiency decreases due to the dielectric loss. As related to water, with a high dielectric constant of 80, dipole antennas placed near it experience a significant shift in their resonant frequency and lose efficiency from not operating at a resonant mode as well as a shift in the antenna impedance negatively impacting the power transfer efficiency [5].

Several studies have been conducted to evaluate the issues of UHF tag readability in relation to metals. One such study conducted a series of experiments to help understand the limitations and opportunities for contributions in passive UHF RFID [4]. It concluded that larger dipole tags yield better performance than smaller tags in conjunction with metal or water. Another study conducted simulations of a half-wave dipole and several modified configurations to serve a basis for analysis of UHF

RFID tag antennas and their potential use in packaging [6]. It concluded that increasing the bandwidth for UHF RFID antennas can compensate for the effects of metal. A study was conducted to disprove the hypothesis that RFID tags cannot be designed to simultaneously operate efficiently in free space and near a conducting surface [7]. The authors of this research presented a new antenna that operates as a dipole when in free space, but when placed on a conducting surface, it operates as a relatively efficient microstrip antenna. To realize the maximum potential for RFID, several researches have designed systems that minimize the effects of nearby conductive objects. Experiments have been performed by placing thin tag antennas on many different types of metals [8], measuring the effect on RFID tag read range in the presence of ground plane [9] and simulating the impedance and gain as an antenna was moved away from a ground plane [10].

As related to packaging, a study evaluated the readability of dipole UHF (866 MHz) tags when applied to Tetra Pak packages that contain aluminum foil in the structure [11]. The combination was tested at individual package and palletized load levels. The dipole antenna was found to be very sensitive to the aluminum foil and modulated scattering power was not sufficient for the reader to read the tag. Another packaging related study explored the effect of aluminum beverage cans on the read range and readability of UHF RFID tags [12]. It was found that the metal cans, with the tags physically visible to the reader antenna or not, interfered with readability. This study also experimented with a corrugated fiberboard spacer between the metal and the tags and found that while this arrangement may increase readability in some situations, it was not very effective.

Metals are used for packaging applications all over the world. The main types of metals used for this purpose are steel (mild steel sheet, tinplate steel and stainless steel) and aluminum [13]. Metal drums and kegs are usually manufactured using mild steel plate, aluminum alloy sheets, commercially pure aluminum sheets and stainless steel; while tinplate, low carbon steel coated on both sides with tin, is used principally for manufacturing metal boxes and cans [13]. Aluminum, often called the transportation metal due to its lighter weight compared to steel, and its alloys are commonly employed to manufacture cans, foil and tubes for packaging applications [13].

Metals, including durable and non durable goods along with containers and packaging, accounted for 8.4% of the total municipal solid waste

generation in the U.S. for 2008 [14]. For the packaging related contribution to this number, steel cans (2,310 thousand tons) and aluminum cans (1,390 thousand tons) were the two major sources [14]. Metals are also commonly used in conjunction with other materials such as multilayer flexible packaging for aseptic packaging, snack bags and antistatic discharge (ESD) bags.

This study was undertaken to evaluate passive UHF RFID tag performance with five commonly used packaging metals, in terms of readability in a three dimensional (3D) read space. The objective of the study was to measure and evaluate the readability of passive UHF RFID tags in conjunction with several commonly used types of metal containing packaging forms. The readability measure was achieved based on three configurations: bare tag, tag attached directly to the metal surface and tag attached to the metal surface with a spacer in a three dimensional read field.

2.0 MATERIALS AND METHODS

2.1 RFID Reader and Antenna

Alien Technology's ALR 9900 RFID reader, an ALR-9611-CR circular polarized antenna and Alien RFID Gateway v. 2.0 were used to conduct this study. The ALR 9900 reader supports all EPC Gen 2 tag protocols for UHF tags operating between 902.25 MHz- 927.25 MHz. It was connected to the host computer using a RS-232 serial connection and its signal strength conformed to the FCC Part 15 guidelines. ALR-9611-CR circular polarized antennas were used because they are less sensitive to tag orientation and they provided the appropriate distances needed for this study [15,16].

2.2 Passive UHF RFID Tags

Five types of tags, promoted by the manufacturers as those that work well in harsh environments, such as in conjunction with conductive and high dielectric materials, were used in this study. Table 1 and Figure 1 describe the tags used in this study. Both the Intermec tags (A and B) had a rugged plastic housing and all three Alien Technology tags (C, D and E) were on label stock.

Table 1. *Passive UHF RFID Tags Used in Study.*

Tag	IC Chip Type	Size (mm)	Recommended Use Environment	Operating Temperature
Intermec, Small Rigid Tag (A)	Impinj Monza	31 × 79	metal, plastic, wood	(–40°C to 121°C)
Intermec, Large Rigid Tag (B)	Impinj Monza	32 × 142.7	metal, plastic, wood	(–40°C to 121°C)
ALN-9654 "G" (C)	Alien Tech. Higgs 3	23.2 × 96.5	high dielectric materials	(–40°C to 70°C)
ALN-9554 "M" (D)	Alien Tech. Higgs 3	32.76 × 98.43	plastic totes, pallets	(–40°C to 70°C)
ALN-9640 "Squiggle" (E)	Alien Tech. Higgs 3	12.31 × 98.18	corrugate, pallets	(–40°C to 70°C)

2.3 Metallic/Metal Containing Packaging

Five types of commonly used packaging either made of metal or containing metallic components were used in this study and are described in Table 2 and Figure 2. The aluminum and tinplate cans as well as the juice box were cut open to construct 27.94 × 17.78 cm flat surfaces. Single layers of the two types of bags used were also cut to this size. The RFID tags were attached at the center on the surfaces, representing the outer side of the packages.

2.4 E-Flute Corrugate Fiberboard Spacer

When tagging RF-opaque or RF-absorbent materials, it is recom-

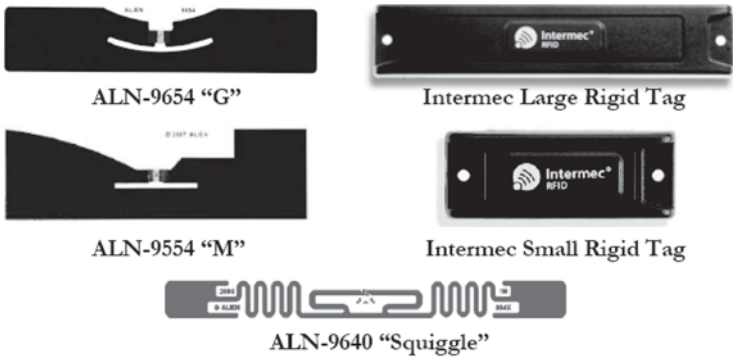

Figure 1. *Passive UHF RFID Tags Used in the Study.*

Figure 2. *Metallic and Metal Containing Packaging Studied.*

mended that the use of a RF-transparent material such as foam or corrugated board can be used to mount the tag on the object [17]. This spacer provides a buffer between the tag and the object and allows the tag antenna to gather and channel the energy to the chip [18]. A past study evaluating the effect of corrugated fiberboard spacer for tagging aluminum cans concluded that this mechanism can improve the readability of the tags [12]. For this study a 1.59 mm thick E-flute corrugated fiberboard material was used as the spacer.

2.5 Methodology

The readability testing was performed as per ASTM D7435 (Standard Test Method for Determining the Performance of Passive Radio Fre-

Table 2. *Metallic and Metal Containing Packaging.*

Packaging	Metal Type	Thickness of Metal Component, μm
Carbonated beverage can (355 mL)	Aluminum	250
Ground coffee can (0.98 kg)	Tinplate steel	340
Metal-in static shielding bag (0.25 m × 0.36 m)	Aluminum foil	8.89
Tetra Pak juice carton (1.9 L)	Aluminum foil	5.82
Snack bag (0.48 kg)	Aluminum foil	17.78

quency Identification (RFID) Transponders on Loaded Containers) [19]. The "read field mapping" procedure identified in this standard is used to determine the read performance of the RF system inclusive of the reader/antenna and transponder with a package. The testing is conducted with the RFID transponder specimen moving both toward and away from the RFID antenna.

The following six variables were included in this study:

- Tag type—Intermec Small Rigid Tag (A), Intermec Large Rigid tag (B), ALN-9654 "G" (C), ALN-9554 "M" (D) and ALN-9640 "Squiggle" (E)
- Packaging type—Aluminum and tinplate cans, static shielding and snack bags and Tetra Pak carton
- Tag configurations—free space, directly attached to package and directly attached to package through a spacer
- Reader attenuations—0, 30 and 60 db
- Read space heights—0 m, +0.91 m and –0.91 m
- Read space angles—0° to 180° in 15° increments

The combinations of tag types and configurations, packaging, attenuation, height and angles amounted to a total of 8775 measurements. The 3D arrangement for the read field measurements is illustrated in Figure 3.

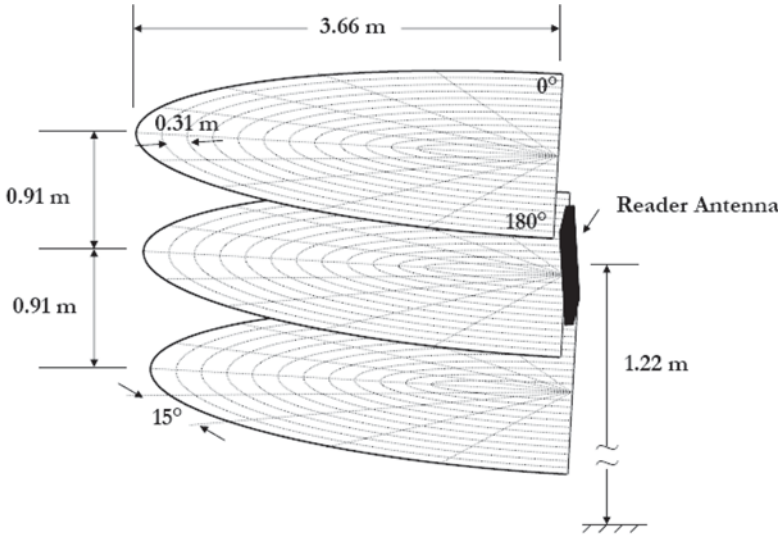

Figure 3. *Experimental Setup for Read Field Measurements.*

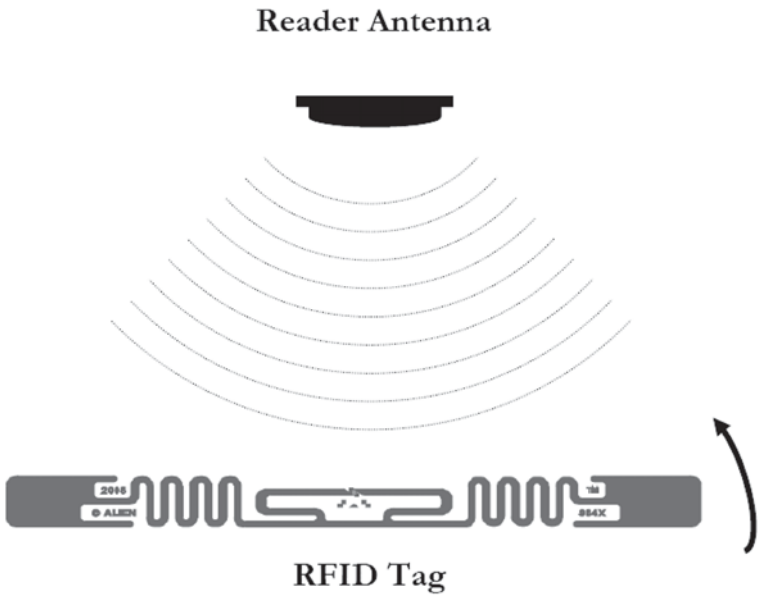

Figure 4. *Movement of RFID Tag in the Read Field.*

The tags were moved in the 3D space in the X-Y plane about the Z-axis as shown in Figure 4. The tag is shown at 0° with respect to the face of the reader antenna. Measurements were made for the read space facing the reader antenna for every 15° at every 30.48 cm distance away from the reader antenna.

The 3D read field volumes were measured relative to the maximum read space assigned for this research (Figure 3). Figures 5, 6, and 7 are included to serve as examples of the read field volumes. To develop these, the polar coordinates were converted to Cartesian coordinates and Mathematica® 7 (Wolfram Research of Champaign, Illinois) was used to create 3D read field graphs.

3.0 RESULTS AND DISCUSSION

To gain insight into the influence of the variables studied as described in Section 2.5, sans the control group, a fixed-effect ANOVA was performed. In this analysis, relative volume was defined as the measured volume relative to maximum volume, where $0 \leq$ relative volume ≤ 1.00. The ANOVA in Table 3 is a mathematical procedure for separating the variability of a group of observations into assignable causes and setting

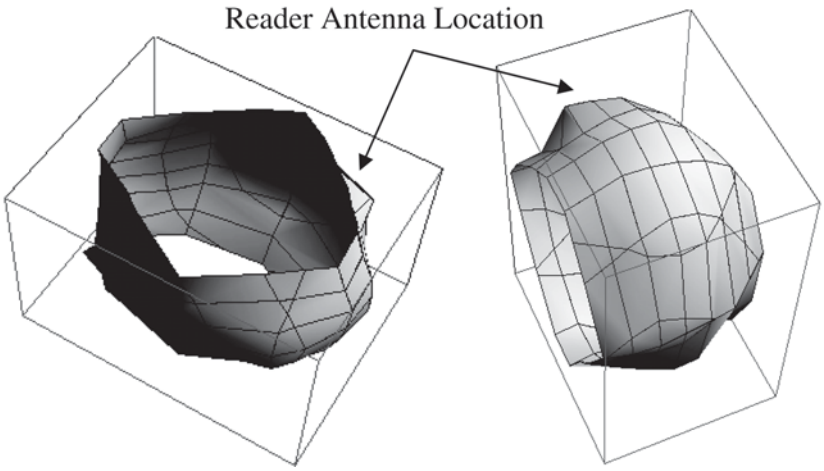

Figure 5. *Read Field Map—Tag A in Free Space at Zero Attenuation.*

up various significance tests. Variability is given by the sums of squares (SS) relative to degrees of freedom (df), this ratio is the mean sums of squares (MS). The corresponding F value is associated with a probability that at least one sample mean in the comparison set is statistically different from at least one other sample mean in the same set.

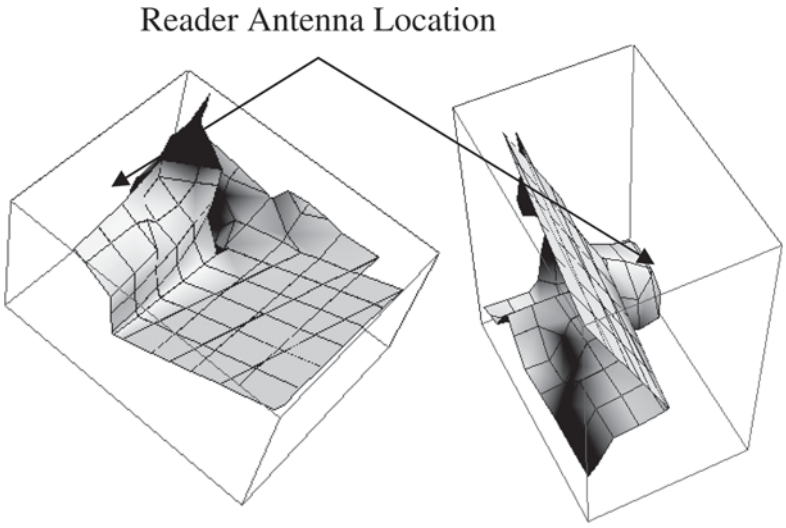

Figure 6. *Read Field Map—Tag A Directly Attached to Aseptic Packaging at Zero Attenuation.*

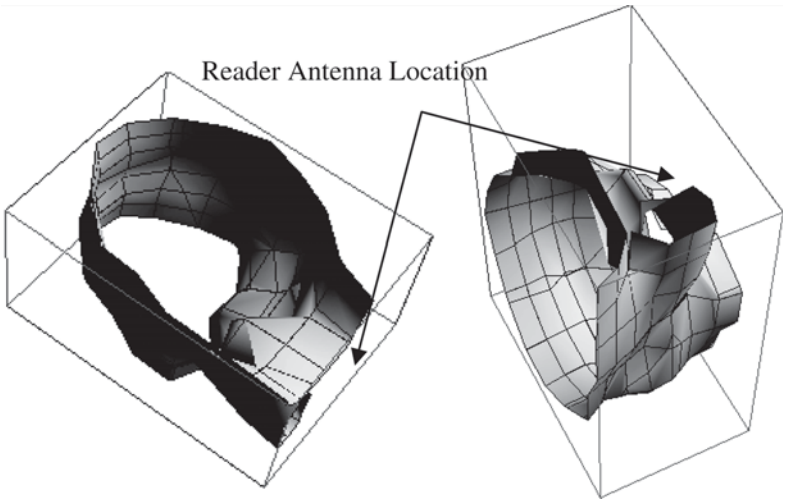

Figure 7. *Read Field Map—Tag A Attached to Aseptic Packaging via a Spacer at Zero Attenuation.*

The results of the ANOVA showed that all four factors (metals, tags, tag configuration and attenuation) had significant effects on read volume. Table 3 shows that all the main effects were statistically significant $p < 0.01$. Of the possible interactions with metals, the key variable, only the metal * tags is significant, $F(12,74) = 35.21, p < 0.001$. Graphic plots

Table 3. *ANOVA of Packaging & Tags, Tag Configurations and Attenuation on Relative Read Field Volume.*

Source	SS	df	MS	*F*	Signif.
Corrected Model	3.44	45	0.074	44.89	<0.001
Intercept	2.20	1	2.204	1334.06	<0.001
Metals (package type)	0.44	4	0.109	66.13	<0.001
Tag Configuration	0.02	1	0.016	9.40	0.003
Attenuation	0.06	2	0.029	17.58	<0.001
Tags	1.94	3	0.647	391.71	<0.001
Metals * Tag Configuration	0.01	4	0.001	0.71	0.589
Metals * Attenuation	0.01	8	0.002	0.95	0.485
Metals * Tags	0.70	12	0.058	35.21	<0.001
Tag Configuration * Attenuation	0.00	2	0.001	0.89	0.414
Tag Configuration * Tags	0.03	3	0.011	6.37	0.001
Attenuation * Tags	0.14	6	0.023	13.67	<0.001
Error	0.12	74	0.002		
Total	**5.66**	**120**			
Corrected Total	**3.46**	**119**			

R Squared = 0.965 (Adjusted R Squared = 0.943)

for metals * tag configuration, metals * attenuation, and metals * tags are presented in Figures 8, 9 and 10 respectively. Figure 11 presents the influence of metals, tag configuration and tags on relative volume.

While the read field volumes were significantly lower in comparison to the tags' performance in free space, the inclusion of a spacer between the tag and packages showed a marked improvement as compared to tags directly attached to the packages (Figure 8). These improvements were 4.56%, 2.31%, 2.17%, 1.14% and 0.93% for the aluminum cans, steel cans, antistatic bags, aseptic packages and snack bags respectively. This verifies the findings from the past study [12].

Attenuation causes the RF energy from the RFID reader to weaken. As seen in Figure 9, except for the steel cans and the snack bags, attenuation of 30 db was the optimum setting towards providing the best read field volumes. This was true for the control (free space) observations as well. The difference between the read field volumes for reader attenuations between 0 and 30 db was the most pronounced for aluminum cans at 1.87%. Attenuation of 60 db provided the lowest read field volumes for all scenarios. These observations may be explained by the facts that the energy emitted by the reader also decreases in proportion to the inverse

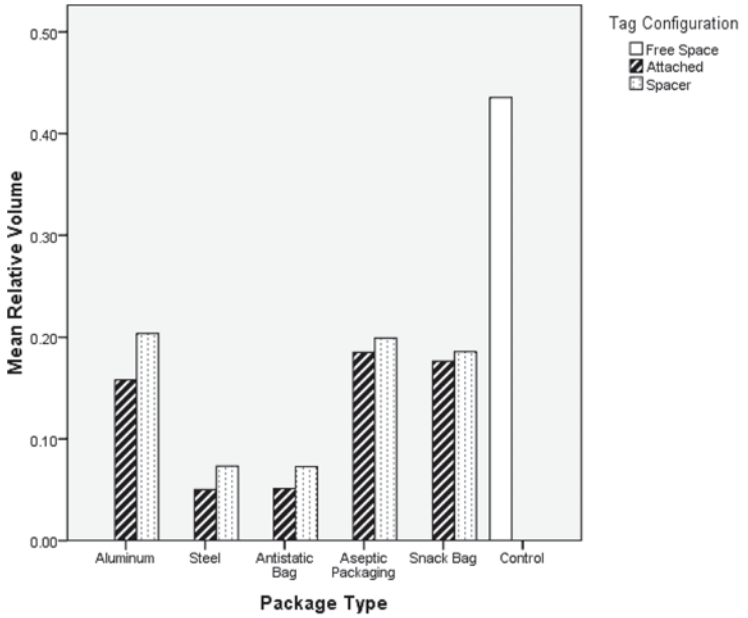

Figure 8. *Relative Read Field Volume by Package Types and Tag Configuration.*

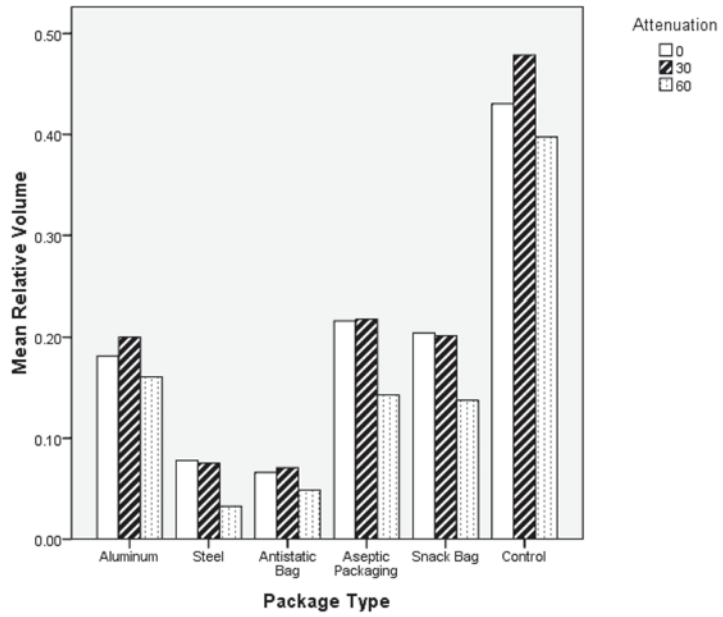

Figure 9. *Relative Read Field Volume by Package Types and Attenuation.*

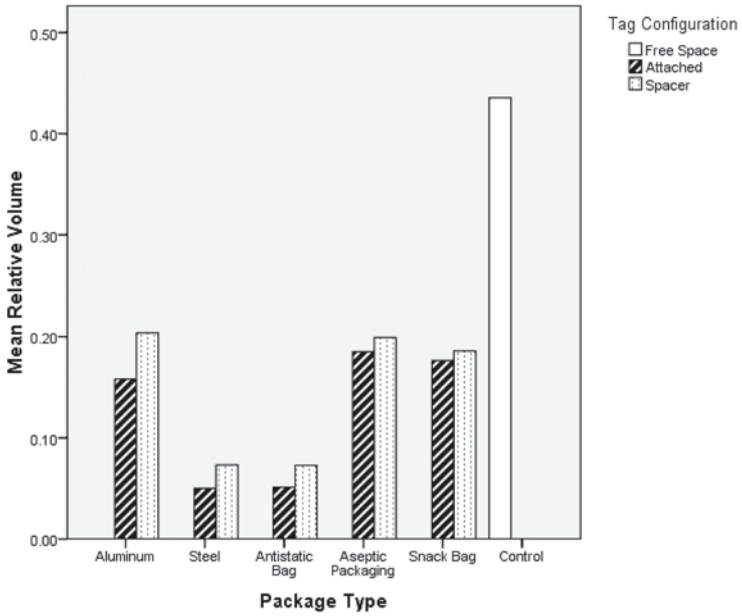

Figure 10. *Relative Read Field Volume by Package and Tag Types.*

square of the distance, passive UHF RFID tags reflect back a signal at very low power levels and that a tag's reflected signal decreases as the inverse fourth power of the distance between tag and reader [5].

Figure 10 illustrates the relative read field volumes for tag types when applied directly to the metallic or metal containing packaging. As compared to control (tags in free space) and tags applied directly to the aluminum cans and aseptic packaging had very similar read field volumes for tag A. Tags C, D and E performed very poorly in comparison to tags A and B. Tag B performed better than the control when fixed to all package types except the antistatic bags and performed better (14.78%) than tag A in conjunction with steel cans.

Figure 11 illustrates the performance of the five tags in free space, when attached directly to the packages and when attached to the packages via the spacer. In free space the tag readability, by tag type in decreasing order, was C > E > A > D > B, while the performance of tags

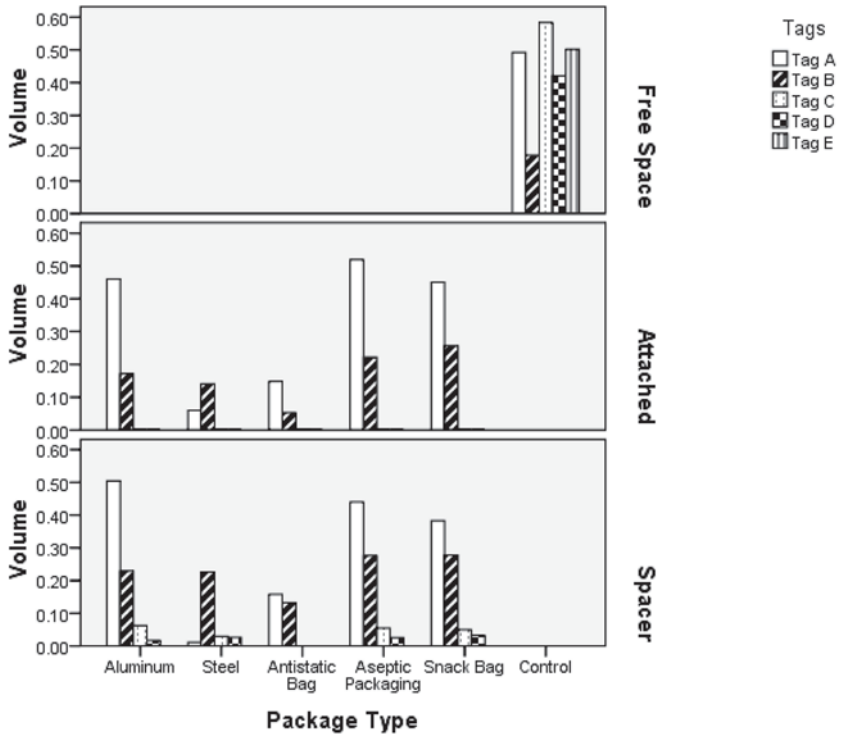

Figure 11. *Relative Read Field Volume by Package & Tag Types and Tag Configuration.*

with metals was A > B > C > D > E. The relative read field volumes by package type for directly affixed tags was ranked in a decreasing order as aseptic packaging snack bag aluminum cans steel cans antistatic bag. It was also observed that the tags dedicated for use with metals (A and B) indeed performed better than those that were not dedicated to it (C, D and E). This could be related to the tag design (IC chip and antenna) as well as the rigid housing for tags A and B.

4.0 CONCLUSIONS

This study evaluated the performance of five passive UHF tags in conjunction with five common packaging forms that use metal in their structure. Using ASTM D7435, over 8775 observations were made to develop relative read field volumes for variables including tag and packaging types, tag configurations and reader attenuation. The study concludes the following:

- Metals cause poor power transfer efficiency between the RFID reader and passive UHF tags.
- All factors used in the experimental plan for this study i.e. tag and packaging types, tag configurations and reader attenuation had significant effects on the read field volumes.
- The inclusion of a spacer between tags and packages can provide marked improvements in readability.
- Attenuating the reader may provide noticeable improvements in readability for some applications.
- Tags marketed to work well in environments containing metal do indeed perform better than those that are not.
- Experimentation is necessary to select the optimum passive UHF tag for use in conjunction with packages containing metals.

REFERENCES

1. K. Michael and L. McCathie. The pros and cons of RFID in supply chain management. *Proc. IEEE Int. Conf. Mobile Business (ICMB),* 2005, pp. 623–629.
2. Sklar, B. Digital Communications: Fundamentals and Applications. Prentice Hall, 2001. ISBN 0-13-084788-7, pages 944–999.
3. Hansen, R. C. Fundamental limitations in antenna. Proc IEEE, Vol. 69, No. 2, pp. 170–182, Feb. 1981.
4. Aroor, S. R., Deavours, D. D. Evaluation of the State of Passive UHF RFID: An Experimental Approach. *IEEE Systems Journal,* 1(2):168–176, Dec 2007.

5. Finkenzeller, K. RFID Handbook: Radio-Frequency Identification Fundamentals and Applications. John Wiley & Sons, New York, NY; ISBN 0-471-98851-0, 1999.
6. T. C. Chau, B. A. Welt, and W. R. Eisentadt, "Analysis and characterization of transponder antennae for radio frequency identification (RFID) systems," Packaging Technology and Science, vol. 19, pp. 33–44, 2006.
7. Naaser A. Mohammed, Mutharasu Sivakumar, and Daniel D. Deavours, An RFID Tag Capable of Free-Space and On-Metal Operation. In *Proc. IEEE Radio and Wireless Symposium* January 18–22, 2009, San Diego, CAPaine, F. A. Packaging User's Handbook. Chapman and Hall, 1991. ISBN 075140151X, pages 81–93.
8. Joshua D. Griffin, Gregory Durgin, Andreas Haldi, and Bernard Kippelen, "Radio Link Budgets for 915MHz RFID Antennas Placed on Various Objects," *WCNG Wireless Symposium, Austin TX,* October 2005.
9. D. M. Dobkin and S. M. Weigand. Environmental Effects on RFID Tag Antennas in *IEEE International Microwave Symposium,* June 2005.
10. P. Raumonen, L. Sydanheimo, L. Ukkonen, M. Keskilammi, M. Kivikoski, "Folded dipole antenna near metal plate," *Antennas and Propagation Society International Symposium,* 2003.
11. Rangapuram, S. R., Persson, N. RFID Compatibility. Master of Science Thesis, Department of Electroscience, Lund University, Sweden. January 2006.
12. Clarke, R. H., Tanprasert, K. Packaging Material Implications in RFID Operations. *Packaging Science and Technology,* Japan. 14(5), pp. 299–315, 2005.
13. Paine, F. A. Packaging User's Handbook. Chapman and Hall, 1996. ISBN 075140151X, pages 81–93.
14. U. S. Environmental Protection Agency, Office of Resource Conservation and Recovery. Municipal Solid Waste Generation, Recycling, and Disposal in the United States—Detailed tables and Figures for 2008.
15. Mc Carthy , U., Ayalew, G., Butler, F., McDonnell, K. and Ward S. The effects of item composition, tag inlay design, reader antenna polarization, power and transponder orientation on the dynamic coupling efficiency of backscatter ultra-high frequency radio frequency identification. *Packaging Technology and Science* 2009; 22 (4): 241–248.
16. Clarke, R., Twede, D., Tazelar, J., Boyer, K. Radio frequency identification (RFID) performance: the effect of tag orientation and package content. *Packaging Technology and Science* 2006; 19 (1): 45–54.
17. Lahiri, S. RFID Sourcebook. IBM Corporation, 2006. ISBN 0131851373, pages 178–179.
18. Philips Semiconductors, TagSys, Texas Instruments Inc. Item Level Visibility in the Pharmaceutical Supply Chain: A Comparison of HF and UHF RFID Technologies. White Paper, July 2004.
19. D7435-08 Standard Test Method for Determining the Performance of Passive Radio Frequency Identification (RFID) Transponders on Loaded Containers. (2008). American Society of Testing and Materials, Volume 15.10, June 2009.

Efficient Gas Injection Algorithms for Use with Active Modified Atmosphere Packaging Machines and Controlled Atmosphere Chambers

WILLIAM PELLETIER[1,*] and KHE V. CHAU[2]

[1]*Ph.D. Candidate, Department of Agricultural and Biological Engineering, IFAS, 290 Frazier-Rogers Hall, PO Box 110570, Gainesville, FL 32611-0570 USA*

[2]*Professor, Department of Agricultural and Biological Engineering, IFAS, Frazier-Rogers Hall, PO Box 110570, Gainesville, FL 32611-0570 USA*

ABSTRACT: Active modified atmosphere packaging (MAP) requires gas flushing to bring initial gas concentrations to desired levels. Respiration of commodities and air leakage inside controlled atmosphere (CA) facilities cause gas concentrations to deviate from set points unless gas mixtures are periodically injected to bring gas concentrations back to the desired set points. This paper presents the complete set of algorithms useful to determine optimal gas injections for active MAP equipment or to bring gas concentrations back to controlled atmosphere set point quickly and effectively. The algorithms are given for all eventualities. Scenarios are described for the case of CA facilities, but they can be in active MAP applications as well. These algorithms were tested on a small-scale chamber and the results corroborated their accuracy.

INTRODUCTION

In the fresh produce industry, controlled atmosphere (CA) storage is widely used in addition to temperature and relative humidity management. Modified atmosphere packaging applications also use flush gasses to rapidly achieve desired gas concentrations in hermetically sealed packages. Kader [1] and Thompson [2] described several advantages of CA storage that contribute to extending shelf life. A large number of scientific papers on CA storage have been published through the years. These publications cover various subjects such as:

*Author to whom correspondence should be addressed. Email: willpell@ufl.edu

1557-7244/10/03 131-24

optimal conditions, gas exchange modeling, fruits and vegetables physiological disorders, sensors technology, etc. However, almost nothing is found in the literature regarding control algorithms for optimal conditions. A CA chamber will always lose the desired gas concentrations with time because of produce respiration, gas exchange through doors and leakage. To maintain desired oxygen (O_2) and carbon dioxide (CO_2) levels, O_2, CO_2 and nitrogen (N_2) must be injected from time to time and some other gases, including ethylene (C_2H_4), have to be scrubbed out. In CA facilities, gas levels have to be maintained accurately at all times. Typically, a control system is used to determine gas concentrations at fixed intervals. Decisions are then made to most efficiently bring these concentrations back to the desired set points. The only recent documents discussing optimal control of gas concentrations were published by Goyette *et al.* [3] and Markarian *et al.* [4]. These publications are complementary work on the same CA storage equipment. In order to control concentrations of O_2 and CO_2 they used two proportional integral controllers (PI). A scrubber was also used in order to remove excess CO_2. Markarian *et al.* [4] also mentioned that their control system re-stabilizes the atmosphere within 48 h of a disturbance. Raghavan *et al.* [5] give a more exhaustive review of the different systems used in modified and controlled atmosphere facilities. They also present an overview of P, PI, PID and fuzzy logic feedback controllers.

In addition to commercial and experimental CA facilities, there are other applications, from various fields, that require control of specific gas concentrations. Development of new modified atmosphere packaging and studies on plant growth in different environmental conditions such as the NASA Mars greenhouse project [6, 7] are examples of these applications.

This paper presents algorithms that can be used to maintain desired gas concentrations efficiently and quickly. The application of these algorithms requires a gas monitoring system (CO_2 and O_2), gas flowmeters, temperature sensor(s) as well as a computer system with monitoring and control capabilities. The algorithms were tested on a small-scale chamber and the results are presented in this paper.

They are intended primarily for use in research facilities that need to maintain gas concentrations at some specified levels. However, they are applicable to any facility or enclosure; use is not restricted to fresh produce applications.

THEORETICAL CONSIDERATIONS

For the purpose of algorithms' development, it is assumed that only O_2 and CO_2 are to be controlled in the facility and that the atmosphere is composed of O_2, CO_2 and N_2. However, the algorithms may also be used to control concentrations of any other two gases and their validity is independent of the nature of the two key gases as well as the nature of any other gases (N_2, CO, H_2O, etc.) that may be present in the environment.

It will be shown that in order to maintain the set points for O_2 and CO_2, it is necessary to inject into the facility only one or two gases but never all three at any one event. In the case where it is necessary to inject two gases, the proposed procedure will inject both gases at the same time and for the same duration. This results in simpler control procedures and faster correction times. The main assumptions behind these algorithms are that the temperature is constant, that gases are well mixed and that gas flow into the chamber is equal to gas flow out in order to maintain atmospheric pressure. The latter assumption implies that an exit valve must be opened during the injection period. In a large facility, the gases should be injected in multiple locations or fans should be used during injection periods to ensure adequate mixing. The basic approach used to develop the algorithms for the various situations is the following:

1. Determine which of the three gases needs to be injected into the CA chamber
2. Solve the mass balance equation for O_2 and CO_2.
3. Set the correction times for O_2 and CO_2 equal to each other and solve for the correct injection mixture.

In practice, eight scenarios were indentified.

SCENARIO 1: BOTH O_2 AND CO_2 CONCENTRATIONS ARE HIGHER THAN THEIR SET POINTS

In this case, N_2 has to be injected to reduce levels of O_2 and CO_2. However, injection of N_2 alone only allows for exact adjustment of O_2 or CO_2 back to set point. Some O_2 or some CO_2 will also need to be injected depending on which gas is predominantly in excess.

1.1 If $\frac{x^0}{x^f} > \frac{y^0}{y^f}$

O_2 is more in excess than CO_2. It will take longer to reduce the O_2 level to its set point than to reduce the level of CO_2 to its set point by the injection of N_2. Therefore, N_2 must be injected along with CO_2 to bring the O_2 and CO_2 levels to their set points at the same time. Injection of N_2 and CO_2 will cause a rate of change in O_2 concentration according to the following equation:

$$-(D_2 + D_3)x = V\frac{dx}{dt} \tag{1}$$

The left side of the equation is equivalent to the flow rate of the O_2 leaving the facility and the right side is the rate of depletion of O_2 inside the facility. Separating the variables:

$$\frac{dx}{x} = -\frac{(D_2 + D_3)}{V}dt \tag{2}$$

Integrating the above equation:

$$t_1 = \frac{V}{D_2 + D_3}\ln\left(\frac{x^0}{x^f}\right) \tag{3}$$

where t_1 is the correction time to bring the O_2 level from x^0 to x^f. Similarly, a mass balance equation for CO_2 may be written as:

$$D_2 - (D_2 + D_3)y = V\frac{dy}{dt} \tag{4}$$

With separation of variables:

$$\frac{dy}{D_2 - (D_2 + D_3)y} = \frac{dt}{V} \tag{5}$$

Upon integration:

$$t_2 = \frac{V}{(D_2 + D_3)}\ln\left(\frac{D_2 - (D_2 + D_3)y^0}{D_2 - (D_2 + D_3)y^f}\right) \tag{6}$$

where t_2 is the correction time to bring the CO_2 level from y^0 to y^f. To find the correct ratio of D_2 and D_3 so that the set points for O_2 and CO_2 are reached at the same time, Equation (3) must be set equal to Equation (6).

After reorganizing the resulting equation, the following relation is obtained:

$$\frac{x^0}{x^f} = \frac{D_2 - (D_2 + D_3)y^0}{D_2 - (D_2 + D_3)y^f} = \frac{\frac{D_2}{D_3} - \left(\frac{D_2}{D_3} + 1\right)y^0}{\frac{D_2}{D_3} - \left(\frac{D_2}{D_3} + 1\right)y^f} \tag{7}$$

Letting $a = D_2/D_3$ and solving Equation (7) for the ratio a:

$$\frac{x^0}{x^f} = \frac{a - (a+1)y^0}{a - (a+1)y^f} \tag{8}$$

$$a = \frac{D_2}{D_3} = \frac{x^0 y^f - x^f y^0}{x^0(1-y^f) - x^f(1-y^0)} = \frac{x^f y^f \left(\frac{x^0}{x^f} - \frac{y^0}{y^f}\right)}{x^0(1-y^f) - x^f(1-y^0)} \tag{9}$$

Once the ratio a is known, the injection time t may be determined by Equations (3) or (6). Therefore, a gas mixture of N_2 and CO_2 at the ratio a must be injected for $t = t_1 = t_2$ seconds to restore the set points. Typically, this is accomplished using two mass flow controllers, one for N_2 and one for CO_2. Analysis of Equation (9) shows that the ratio a will always be positive (Appendix 1). This indicates that the procedure will always successfully restore the gas levels to their set points.

1.2 If $\frac{x^0}{x^f} < \frac{y^0}{y^f}$

CO_2 is more in excess than O_2. N_2 and some O_2 must therefore be injected. A mass balance equation for O_2 may be written as:

$$D_1 - (D_1 + D_3)x = V\frac{dx}{dt} \tag{10}$$

Separating the variables:

$$\frac{dx}{D_1 - (D_1 + D_3)x} = \frac{dt}{V} \tag{11}$$

Upon integration:

$$t_1 = \frac{V}{D_1 + D_3} \ln\left(\frac{D_1 - (D_1 + D_3)x^0}{D_1 - (D_1 + D_3)x^f}\right) \tag{12}$$

where t_1 is the correction time to bring the O_2 level from x^0 to x^f. Similarly, a mass balance equation for CO_2 may be written as:

$$-(D_1 + D_3)y = V\frac{dy}{dt} \tag{13}$$

$$\frac{dy}{y} = -\frac{(D_1 + D_3)}{V}dt \tag{14}$$

Upon integration:

$$t_2 = \frac{V}{D_1 + D_3} \ln\left(\frac{y^0}{y^f}\right) \tag{15}$$

where t_2 is the correction time to bring the CO_2 level from y^0 to y^f. To find the correct ratio of D_1 and D_3, so that the set points for O_2 and CO_2 are reached at the same time, Equation (12) must be set equal to equation (15) and then solve for the ratio $a = D_1/D_3$:

$$a = \frac{D_1}{D_3} = \frac{x^f y^0 - x^0 y^f}{y^0(1 - x^f) - y^f(1 - x^0)} = \frac{x^f y^f\left(\frac{y^0}{y^f} - \frac{x^0}{x^f}\right)}{y^0(1 - x^f) - y^f(1 - x^0)} \tag{16}$$

Once the ratio a is known, the injection time may be determined using either Equation (12) or (15). Analysis of Equation (16) also shows that the ratio will always be positive (Appendix 1).

1.3 If $\frac{x^0}{x^f} = \frac{y^0}{y^f}$

Only N_2 needs to be injected to bring both O_2 and CO_2 to their set points. A mass balance equation for O_2 may be written as:

$$-D_3 x = V\frac{dx}{dt} \tag{17}$$

and upon integration:

$$t_1 = \frac{V}{D_3} \ln\left(\frac{x^0}{x^f}\right) \tag{18}$$

Similarly, the mass balance equation for CO_2 will give:

$$-D_3 y = V \frac{dy}{dt} \tag{19}$$

$$t_2 = \frac{V}{D_3} \ln\left(\frac{y^0}{y^f}\right) \tag{20}$$

Since $x^0/x^f = y^0/y^f$, Equations (18) and (20) are equal, i.e. $t_1 = t_2$. In other words, injecting N_2 at a constant rate D_3 for a period $t = t_1 = t_2$ will bring both O_2 and CO_2 to their set points.

SCENARIO 2: O_2 CONCENTRATION IS HIGHER THAN ITS SET POINT AND THE CO_2 CONCENTRATION IS EQUAL TO ITS SET POINT

In this case, a mixture of N_2 and CO_2 must be injected. Since CO_2 is already at its set point, the concentration of CO_2 in the injection mixture must be equal to its set point y^f:

$$\frac{D_2}{D_2 + D_3} = y^f \tag{21}$$

Substituting $a = D_2/D_3$ in Equation (21):

$$a = \frac{D_2}{D_3} = \frac{y^f}{1 - y^f} \tag{22}$$

With this mixture, only the change of O_2 with time needs to be investigated. The mass balance equation for O_2 is:

$$-(D_2 + D_3)x = V \frac{dx}{dt} \tag{23}$$

The injection time can be calculated from:

$$t_1 = \frac{V}{D_2 + D_3} \ln\left(\frac{x^0}{x^f}\right) \tag{24}$$

Therefore, by selecting the desired flow rate of either CO_2 or N_2, the

ratio a given by Equation (22) will determine the other. To complete the procedure, both gases must be injected simultaneously, at respective flow rates, over a period given by the injection time of Equation (24).

SCENARIO 3: THE O_2 CONCENTRATION IS EQUAL TO ITS SET POINT AND THE CO_2 CONCENTRATION IS HIGHER THAN ITS SET POINT

This scenario is similar to **Scenario 2**, except that O_2 and CO_2 are interchanged. Therefore, N_2 and O_2 need to be injected in this case. For this scenario, the ratio a is defined by Equation (25).

$$a = \frac{D_1}{D_3} = \frac{x^f}{1 - x^f} \tag{25}$$

The resulting injection time is provided by Equation (26).

$$t_2 = \frac{V}{D_1 + D_3} \ln\left(\frac{y^0}{y^f}\right) \tag{26}$$

SCENARIO 4: O_2 CONCENTRATION IS LOWER THAN ITS SET POINT AND THE CO_2 CONCENTRATION IS EQUAL TO ITS SET POINT

O_2 and CO_2 must be injected and since CO_2 concentration is already equal to its set point, the CO_2 concentration of the mixture must be equal to its set point y^f.

$$\frac{D_2}{D_1 + D_3} = y^f \tag{27}$$

if $a = D_1/D_2$ therefore:

$$a = \frac{1 - y^f}{y^f} \tag{28}$$

The mass balance equation for O_2 and the injection time are therefore given by:

$$D_1 - (D_1 + D_2)x = V\frac{dx}{dt} \tag{29}$$

$$t_1 = \frac{V}{D_1 + D_2} \ln\left(\frac{D_1 - (D_1 + D_2)x^0}{D_1 - (D_1 + D_2)x^f}\right) \tag{30}$$

SCENARIO 5: O_2 CONCENTRATION IS EQUAL TO ITS SET POINT AND CO_2 CONCENTRATION IS LOWER THAN ITS SET POINT

This is similar to **Scenario 4** except that O_2 and CO_2 are interchanged. Therefore, O_2 and CO_2 must be injected. For this scenario, the ratio a is defined by Equation (31).

$$a = \frac{D_1}{D_2} = \frac{x^f}{1 - x^f} \tag{31}$$

The resulting injection time is provided by Equation (32).

$$t_2 = \frac{V}{D_1 + D_2} \ln\left(\frac{D_2 - (D_1 + D_2)y^0}{D_2 - (D_1 + D_2)y^f}\right) \tag{32}$$

SCENARIO 6: O_2 CONCENTRATION IS LOWER THAN ITS SET POINT AND CO_2 CONCENTRATION IS LOWER THAN ITS SET POINT

O_2 and CO_2 must to be injected in order to raise the concentration of both of these gases. Mass balance for O_2 gives:

$$D_1 - (D_1 + D_2)x = V\frac{dx}{dt} \tag{33}$$

Upon integration:

$$t_1 = \frac{V}{D_1 + D_2} \ln\left(\frac{D_1 - (D_1 + D_2)x^0}{D_1 - (D_1 + D_2)x^f}\right) \tag{34}$$

Mass balance equation for CO_2 gives:

$$D_2 - (D_1 + D_2)y = V\frac{dy}{dt} \tag{35}$$

and upon integration:

$$t_2 = \frac{V}{D_1 + D_2} \ln\left(\frac{D_2 - (D_1 + D_2)y^0}{D_2 - (D_1 + D_2)y^f}\right) \tag{36}$$

To find the right mixture $a = D_1/D_2$, equations for t_1 and t_2 are set equal to each other and then solve for the ratio a:

$$\frac{D_1 - (D_1 + D_2)x^0}{D_1 - (D_1 + D_2)x^f} = \frac{D_2 - (D_1 + D_2)y^0}{D_2 - (D_1 + D_2)y^f} \tag{37}$$

$$\frac{a - (a+1)x^0}{a - (a+1)x^f} = \frac{1 - (a+1)y^0}{1 - (a+1)y^f} \tag{38}$$

After simplification of Equation (38) the following ratio is obtained:

$$a = \frac{D_1}{D_2} = \frac{x^f(1 - y^0) - x^0(1 - y^f)}{y^f(1 - x^0) - y^0(1 - x^f)} \tag{39}$$

From Equation (39), the ratio a is never negative and that procedure will always provide proper corrections using the ratio a with an injection time of $t = t_1 = t_2$ (Appendix 1).

SCENARIO 7: O_2 CONCENTRATION IS HIGHER THAN ITS SET POINT AND CO_2 CONCENTRATION IS LOWER THAN ITS SET POINT

In this situation, a preliminary analysis suggests that CO_2 and N_2 must be injected. This process is governed by the same mass balance equations as **Scenario 1.1**. The ratio a and the injection time are given by:

$$a = \frac{D_2}{D_3} = \frac{x^0 y^f - x^f y^0}{x^0(1 - y^f) - x^f(1 - y^0)} = \frac{x^f y^f \left(\frac{x^0}{x^f} - \frac{y^0}{y^f}\right)}{x^0(1 - y^f) - x^f(1 - y^0)} \tag{40}$$

$$t_1 = \frac{V}{D_2 + D_3} \ln\left(\frac{x^0}{x^f}\right) \tag{41}$$

Given the values of x^0, x^f, y^0 and y^f of **Scenario 7**, the numerator of the right hand side of Equation (40) will always be positive (Appendix 1).

The sign of the ratio a depends only of the denominator in equation (40). An analysis of the denominator shows that three different scenarios are possible whereas only one scenario was possible for **Scenario 1.1** (Appendix 1).

7.1 The Denominator is Positive: $\frac{1 - y^0}{1 - y^f} < \frac{x^0}{x^f}$

In this case, the ratio a is well defined. CO_2 and N_2 are to be injected according to Equations (40) and (41).

7.2 The Denominator is Zero: $\frac{1 - y^0}{1 - y^f} = \frac{x^0}{x^f}$

Equation (40) shows that D_3 is equal to zero in this case. The fact that D_3 is zero does not affect the validity of Equation (41), which will provide the correction time for any pure CO_2 injection flow rate D_2.

7.3 The Denominator is Negative: $\frac{1 - y^0}{1 - y^f} > \frac{x^0}{x^f}$

Equations (40) and (41) cannot be used because the ratio a is now negative. Rearranging the denominator of Equation (40), it becomes,

$$\frac{z^0}{z^f} > \frac{x^0}{x^f}$$

which means that the proportion of O_2 in excess is smaller than the proportion of N_2 in excess (Appendix 1). Even if pure CO_2 is injected, by the time the excess in O_2 is corrected, the CO_2 is not yet corrected. In order to make the corrections, O_2 and CO_2 need to be injected and therefore the equations presented in **Scenario 6** must be used. It can be shown that this procedure will always be successful with the concentrations x^0, x^f, y^0 and y^f associated with **Scenario 7.3** (Appendix 1).

SCENARIO 8: O_2 CONCENTRATION IS LOWER THAN ITS SET POINT AND CO_2 CONCENTRATION IS HIGHER THAN ITS SET POINT

This scenario is similar to **Scenario 7**, except that O_2 and CO_2 are interchanged. Therefore, assuming that O_2 and N_2 need to be injected, this

scenario is governed by the same mass balance equations as **Scenario 1.2**:

$$a = \frac{D_1}{D_3} = \frac{x^f y^0 - x^0 y^f}{y^0(1-x^f) - y^f(1-x^0)} = \frac{x^f y^f \left(\frac{y^0}{y^f} - \frac{x^0}{x^f}\right)}{y^0(1-x^f) - y^f(1-x^0)} \quad (42)$$

$$t_2 = \frac{V}{D_1 + D_3} \ln\left(\frac{y^0}{y^f}\right) \quad (43)$$

Given the values of x^0, x^f, y^0 and y^f of **Scenario 8**, the numerator of the right hand side of Equation (42) will always be positive (Appendix 1). Depending of the denominator of Equation (42), three scenarios are possible.

8.1 The Denominator is Positive: $\frac{1-x^0}{1-x^f} < \frac{y^0}{y^f}$

To correct the gas concentrations, O_2 and N_2 are to be injected according to Equations (42) and (43).

8.2 The Denominator is Zero: $\frac{1-x^0}{1-x^f} = \frac{y^0}{y^f}$

Equation (42) shows that D_3 is equal to zero in this case. O_2 is to be injected according to Equation (43).

8.3 The Denominator is Negative: $\frac{1-x^0}{1-x^f} > \frac{y^0}{y^f}$

Equations (42) and (43) cannot be used because the ratio a is negative. Rearranging the denominator of Equation (42), it becomes,

$$\frac{z^0}{z^f} > \frac{y^0}{y^f}$$

which means that the proportion of CO_2 in excess is smaller than the proportion of N_2 in excess (Appendix 1). As it was discussed in **Scenario 7.3**, O_2 and CO_2 need to be injected and therefore the equations presented in **Scenario 6** must be used. This procedure will always be successful with the concentrations x^0, x^f, y^0 and y^f associated with **Scenario 8.3** (Appendix 1). A summary of all scenarios is presented in Table 1.

Table 1. *Summary of the Algorithms.*

	Scenario	Criteria	Ratio *a*	Time - *t*
1.1	O_2 and CO_2 are higher than set points	$\frac{x^0}{x^f} > \frac{y^0}{y^f}$	$\frac{D_2}{D_3} = \frac{x^f y^f \left(\frac{x^0}{x^f} - \frac{y^0}{y^f}\right)}{x^0(1-y^f) - x^f(1-y^0)}$	$\frac{V}{D_2+D_3}\ln\left(\frac{x^0}{x^f}\right)$ OR $\frac{V}{D_2+D_3}\ln\left(\frac{D_2-(D_2+D_3)y^0}{D_2-(D_2+D_3)y^f}\right)$
1.2		$\frac{x^0}{x^f} < \frac{y^0}{y^f}$	$\frac{D_1}{D_3} = \frac{x^f y^f \left(\frac{y^0}{y^f} - \frac{x^0}{x^f}\right)}{y^0(1-x^f) - y^f(1-x^0)}$	$\frac{V}{D_1+D_3}\ln\left(\frac{D_1-(D_1+D_3)x^0}{D_1-(D_1+D_3)x^f}\right)$ OR $\frac{V}{D_1+D_3}\ln\left(\frac{y^0}{y^f}\right)$
1.3		$\frac{x^0}{x^f} = \frac{y^0}{y^f}$	Inject N_2 Only	$\frac{V}{D_3}\ln\left(\frac{x^0}{x^f}\right)$ OR $\frac{V}{D_3}\ln\left(\frac{y^0}{y^f}\right)$

(continued)

Table 1 (continued). *Summary of the Algorithms.*

	Scenario	Criteria	Ratio *a*	Time - *t*
2	O_2 is higher than set point and CO_2 is equal to its setpoint	—	$\frac{D_2}{D_3}=\frac{y^f}{1-y^f}$	$\frac{V}{D_2+D_3}\ln\left(\frac{x^0}{x^f}\right)$
3	O_2 is equal to its set point and CO_2 is higher than its set point	—	$\frac{D_1}{D_3}=\frac{x^f}{1-x^f}$	$\frac{V}{D_1+D_3}\ln\left(\frac{y^0}{y^f}\right)$
4	O_2 is lower than its set point and CO_2 is equal to its set point	—	$\frac{D_1}{D_2}=\frac{1-y^f}{y^f}$	$\frac{V}{D_1+D_2}\ln\left(\frac{D_1-(D_1+D_2)x^0}{D_1-(D_1+D_2)x^f}\right)$
5	O_2 is equal to its set point and CO_2 is lower than its set point	—	$\frac{D_1}{D_2}=\frac{x^f}{1-x^f}$	$\frac{V}{D_1+D_2}\ln\left(\frac{D_2-(D_1+D_2)y^0}{D_2-(D_1+D_2)y^f}\right)$
6	O_2 is lower than its set point and CO_2 is lower than its set point	—	$\frac{D_1}{D_2}=\frac{x^f(1-y^0)-x^0(1-y^f)}{y^f(1-x^0)-y^0(1-x^f)}$	$\frac{V}{D_1+D_2}\ln\left(\frac{D_1-(D_1+D_2)x^0}{D_1-(D_1+D_2)x^f}\right)$ OR $\frac{V}{D_1+D_2}\ln\left(\frac{D_2-(D_1+D_2)y^0}{D_2-(D_1+D_2)y^f}\right)$

(continued)

Table 1 (continued). *Summary of the Algorithms.*

	Scenario	Criteria	Ratio *a*	Time - *t*
7.1	O_2 is higher than its set point and CO_2 is lower than its set point	$\frac{1-y^0}{1-y^f} < \frac{x^0}{x^f}$	Use Scenario 1.1	
7.2		$\frac{1-y^0}{1-y^f} = \frac{x^0}{x^f}$	Use Scenario 1.1	
7.3		$\frac{1-y^0}{1-y^f} > \frac{x^0}{x^f}$	Use Scenario 6	
8.1	O_2 is lower than its set point and CO_2 is higher than its set point	$\frac{1-x^0}{1-x^f} < \frac{y^0}{y^f}$	Use Scenario 1.2	
8.2		$\frac{1-x^0}{1-x^f} = \frac{y^0}{y^f}$	Use Scenario 1.2	
8.3		$\frac{1-x^0}{1-x^f} > \frac{y^0}{y^f}$	Use Scenario 6	

MATERIAL AND METHODS

In order to test the algorithms, a cylindrical chamber with a void space of 0.01495 m³ was used. A magnetic agitator was placed within the chamber to assure uniform mixing. A valve was opened during the injection period in order to maintain a constant pressure within the chamber. Three mass flow controllers (M100B, MKS Instruments, Inc., MA) were used. The controllers for O_2, CO_2 and N_2 had a range and precision (in standard conditions) of 0 to 8.27×10^{-6} m³/s and $\pm 0.09 \times 10^{-6}$ m³/s for O_2, 0 to 1.17×10^{-6} m³/s and $\pm 0.01 \times 10^{-6}$ m³/s for CO_2 and 0 to 16.7×10^{-6} m³/s and $\pm 0.2 \times 10^{-6}$ m³/s for N_2. The flow of each gas was controlled using a computer. All tests were conducted at 23°C. Concentrations of O_2 and CO_2 in the chamber were measured through a septum using a head space analyzer (CheckMate 9900, PBI Dansensor, Denmark). The accuracy of the gas analyzer was ±1% (of the reading) for O_2 and ±2% (full scale, 0 to 100%) for CO_2.

The different scenarios were combined to six different types (Table 2). Scenarios with the same mathematical algorithms, but with O_2 and CO_2 transposed were grouped under a single type. For example, **Scenario 2** (O_2 is higher than its set point and CO_2 is equal to its set point) and **Scenario 3** (O_2 is equal to its set point and CO_2 is higher than its set point) are considered as being of the same type. Three repetitions were made for every type of algorithm for a total of 18 tests. The initial conditions were arbitrarily set for each test. For the Type f algorithms (**Scenarios 7** and **8**), only **Scenarios 7.1** and **8.1** were tested since **Scenarios 7.2**, **7.3**, **8.2** and **8.3** already corresponded to other scenarios to be tested. Maximum airflows, according to the required ratio *a*, were selected to obtain the shortest injection time possible. For simplicity, set points for every test were 10% CO_2 and 10% O_2. Accuracy of the algorithms depended on the accuracy of temperature, pressure and gas concentration

Table 2. *Types of Algorithms.*

Type	Scenarios
a	1.1 & 1.2
b	1.3 & 7.2 & 8.2
c	2 & 3
d	4 & 5
e	6 & 7.3 & 8.3
f	7.1 & 8.1

measurements, not on their magnitude. Other factors regarding accuracy of algorithms are uncertainty associated with the assumptions discussed previously, the void volume calculations and accuracy of flow controllers used for gas injection (O_2, CO_2 and N_2). However, as mentioned by Bishop [8] and Jameson [9] the success of an automated control system relies mostly on the accuracy and reliability of the gas monitoring equipments (O_2 and CO_2).

RESULTS AND DISCUSSION

Accuracy of the Corrections

Table 3 presents results of all tests with set points at 10% O_2 and 10% CO_2. Results revealed a high accuracy for corrections achieved using the algorithms. This is particularly true for the final O_2 concentration. The higher accuracy of the O_2 sensor compared to the CO_2 sensor is reflected in the better control for O_2 than CO_2. Differences between final corrected concentrations and set points were, except in one case, within the measurement accuracy of the head space analyzer used (Table 3). It is important to mention that injection time depends only on the capacity of the flow controllers (i.e. the higher the flow rate, the shorter the injection time). Depending on the void space it is possible to correct the gas concentration within seconds or minutes.

Algorithms' Effectiveness

To illustrate the effectiveness of the proposed approach, consider the case of purging a container to bring it to the set point concentrations. A chamber is often purged to set the initial gas concentrations in CA applications. Typically, this is performed by flushing the container with the desired final mixture. The following section will show that the proposed algorithms will require much less gas than the traditional procedure.

Injection at a constant flow rate (D) of gas mixture with a fixed composition in a constant volume (V) chamber was considered.

Also, it was assumed that the gas within the chamber was well mixed so that the gas coming out of the chamber has the same composition as the gas within the chamber. From a mass balance on one gas of the mixture, an equation of the change with time of that gas concentration can be obtained (Appendix 2).

Table 3. *Results of the Tests for All Types of Algorithms.*

Type	Scenario	Test	Time (s)	Gas Flow O_2 10^{-6} m^3/s	Gas Flow CO_2 10^{-6} m^3/s	Gas Flow N_2 10^{-6} m^3/s	Volume 10^{-6} m^3/s	Initial Concentration O_2 %	Initial Concentration CO_2 %	Final Concentrations O_2 %	Final Concentrations CO_2 %
a	1.1	1	325	0	1.27	17.4	6067.8	15.0	11.6	10.1	10.4
		2	343	0	1.01	18.1	6554.7	15.5	12.6	10.0	10.4
		3	376	0	0.81	18.1	7110.2	16.1	13.5	10.0	10.4
b	1.3	1	335	0	0	18.1	6063.5	15.0	15.0	10.1	10.5
		2	278	0	0	18.1	5031.8	14.0	14.0	10.1	10.4
		3	223	0	0	18.1	4036.3	13.1	13.1	10.0	10.2
c	2	1	175	0	1.27	11.4	2217.3	11.6	10.0	10.0	10.3
		2	509	0	1.27	11.4	6449.0	15.4	10.2	10.0	10.6
		3	413	0	1.27	11.4	5232.7	14.2	10.2	10.0	10.5
d	4	1	55	8.99	0.99	0	548.9	7.0	10.0	10.0	10.1
		2	67	8.99	0.99	0	668.7	6.3	10.0	10.0	10.0
		3	36	8.99	0.99	0	359.3	8.0	10.0	9.9	10.0
e	6	1	447	0.55	1.27	0	813.5	8.9	6.7	10.1	10.1
		2	553	1.38	1.27	0	1465.5	5.7	6.1	10.1	10.4
		3	265	2.1	1.27	0	895.7	6.8	8.3	10.0	10.2
f	7.1	1	676	0	1.27	7.2	5725.7	14.7	7.7	9.8	10.5
		2	691	0	1.27	6.8	5576.4	14.5	7.4	9.9	10.5
		3	691	0	1.27	6.8	5576.4	14.5	7.4	10.0	10.5

$$x = x_m + (x_0 - x_m)e^{-\frac{D}{V}t} \tag{44}$$

In Equation (44), x_m is the volumetric concentration of the given gas in the injected mixture, x^0 the initial volumetric concentration in the chamber and x the volumetric concentration at a given time t in the chamber. Equation (44) shows that when the product Dt of the exponential term approaches a value of about $6V$ ($e^{-6} \approx 0.0025$) the concentration in the chamber is within 0.2 percentage point of the concentration of the injection mixture. This means that using the chamber purge technique, an amount of gas equal to 6 times or more the volume of the chamber must be injected to correct the gas concentrations.

Using the proposed algorithms, consider a 1 m^3 chamber at 23°C with the following initial concentrations and set points: $x^0 = 0.1$, $y^0 = 0.15$ $x^f = 0.05$ $y^f = 0.1$.

Since $x^0/x^f > y^0/y^f$, this situation corresponds to Scenario 1.1. The results of the algorithm indicate that a volume of 0.66 m^3 of N_2 and a volume of 0.035 m^3 of CO_2 must be injected to correct the concentrations. This is a total of about 0.695 m^3, compared to 6 m^3 for the case where the chamber would have been purged. This represents an economy of gas of 88.4% that clearly highlights the effectiveness of the algorithms presented here.

When a chamber is to be purged of 100% of a gas (O_2, CO_2 or N_2), the algorithms presented here cannot be used. To correct the gas concentrations, it must be purged with a minimum of "six volumes" of the desired final gas mixture as described above.

Comments on the Application of the Algorithms

The gas sampling or monitoring rate depends on several factors such as the volume of the chamber/room, leakage, product respiration rate, etc. If the respiration and leakage rates are known, it is possible to calculate the rate of change of the gas levels in the facility and therefore determine the appropriate sampling rate. If not, the sampling or monitoring rate can be arbitrarily set at 30 min for example, and after a few hours, the computer can reset the sampling rate to maintain the set points within the specified tolerance levels. It is important to mention that the cause of the deviation from the gas concentration set points is irrelevant to the use of the algorithms.

CONCLUSION

CA storage and active MAP have been used for several years in fresh produce industry. However, through the years almost no scientific work has been published regarding methods to effectively maintain the optimal gas concentrations in storage chambers. The objective of this paper was to develop algorithms that can be implemented on any simple control systems in order to bring the gas concentrations of a CA storage room to their set points. All possible scenarios were considered. The algorithms were tested on a small-scale chamber and results were excellent. For all tests, a relatively short injection time as well as a small amount of gas was required in order to reach the set points. Such results are expected for any industrial or experimental applications where the algorithms may be used.

APPENDIX 1—PROOFS OF CONVERGENCE

Scenario 1.1: $\boldsymbol{x^0 > x^f}$ **,** $\boldsymbol{y^0 > y^f}$ **,** $\boldsymbol{\dfrac{x^0}{x^f} > \dfrac{y^0}{y^f}}$

$$a = \frac{D_2}{D_3} = \frac{x^0 y^f - x^f y^0}{x^0(1-y^f) - x^f(1-y^0)} = \frac{x^f y^f \left(\dfrac{x^0}{x^f} - \dfrac{y^0}{y^f}\right)}{x^0(1-y^f) - x^f(1-y^0)}$$

The numerator is positive since: $x^f > 0$, $y^f > 0$ and $\dfrac{x^0}{x^f} > \dfrac{y^0}{y^f}$.

The denominator is positive since: $x^0 > x^f$ and $(1 - y^f) > (1 - y^0)$. The denominator can never be zero. The expression for the ratio a is therefore always positive. The same conclusion is also be obtained by observation that a is the ratio of the injection rates of CO_2 and N_2, and that both gases must be injected in this case, the ratio of their injection rates is required to be positive.

All proofs associated with **Scenario 1.1** may be applied to **Scenario 1.2** by interchanging the O_2 and the CO_2 levels.

Scenario 6: $\boldsymbol{x^0 < x^f}$**,** $\boldsymbol{y^0 < y^f}$

$$a = \frac{D_1}{D_2} = \frac{x^f(1-y^0) - x^0(1-y^f)}{y^f(1-x^0) - y^0(1-x^f)}$$

The numerator is positive since: $x^f > x^0$ and $(1 - y^0) > (1 - y^f)$

The denominator is positive since: $y^f > y^0$ and $(1 - x^0) > (1 - x^f)$

The expression for the ratio a is therefore always positive. Using a different approach, since *a* is the ratio of the injection rates of O_2 and CO_2 and that both O_2 and CO_2 are in deficit: both gas will need to be injected and therefore D_1, D_2 and a are always positive.

Scenario 7: $x^0 > x^f$, $y^0 < y^f$

$$a = \frac{D_2}{D_3} = \frac{x^0 y^f - x^f y^0}{x^0(1-y^f) - x^f(1-y^0)} = \frac{x^f y^f \left(\frac{x^0}{x^f} - \frac{y^0}{y^f}\right)}{x^0(1-y^f) - x^f(1-y^0)}$$

Since $x^0/x^f > 1$ and $y^0/y^f < 1$, the numerator of the ratio a is always positive in **Scenario 7**. This implies that D_2 (the numerator of a and the injection rate of CO_2) cannot be zero.

Scenorio 7.3: The Denominator is Negative: $\dfrac{\mathbf{1 - y^0}}{\mathbf{1 - y^f}} > \dfrac{\mathbf{x^0}}{\mathbf{x^f}}$

Since $1 = x^0 + y^0 + z^0 = x^f + y^f + z^f$, the latter equation can be rewritten as:

$$\frac{1-y^0}{1-y^f} = \frac{x^0 - z^0}{x^f - z^f} > \frac{x^0}{x^f}$$

Using the following mathematical identity:

$$\text{if} \quad \frac{a}{b} < \frac{c}{d} \quad \text{then} \quad \frac{a+c}{b+d} < \frac{a}{b}$$

Therefore

$$\frac{x^0 + z^0}{x^f + z^f} > \frac{x^0}{x^f} \Rightarrow \frac{z^0}{z^f} > \frac{x^0}{x^f}$$

Even if pure CO_2 is being injected, excess O_2 will be corrected before excess N_2. In other words, the concentration of O_2 will be corrected but there will still be too much N_2, which implies a deficiency in CO_2. O_2 and CO_2 need to be injected in this case, therefore **Scenario 6** needs to be used. The ratio *a* is given by:

$$a = \frac{D_1}{D_2} = \frac{x^f(1-y^0) - x^0(1-y^f)}{y^f(1-x^0) - y^0(1-x^f)}$$

Using $1 = x^0 + y^0 + z^0 = x^f + y^f + z^f$, it can be rewritten as:

$$a = \frac{D_1}{D_2} = \frac{x^f(x^0 + z^0) - x^0(x^f + z^f)}{y^f(y^0 + z^0) - y^0(y^f + z^f)} = \frac{x^f x^0 + x^f z^0 - x^0 x^f - x^0 z^f}{y^f y^0 + y^f z^0 - y^0 x^f - y^0 z^f}$$

$$a = \frac{D_1}{D_2} = \frac{x^f z^0 - x^0 z^f}{y^f z^0 - y^0 z^f} = \frac{x^f z^f \left(\frac{z^0}{z^f} - \frac{x^0}{x^f}\right)}{y^f z^f \left(\frac{z^0}{z^f} - \frac{y^0}{y^f}\right)}$$

Since

$$\frac{z^0}{z^f} > \frac{x^0}{x^f} > \frac{y^0}{y^f}$$

in **Scenario 7.3**, the numerator and denominator of the latter equation, and therefore the ratio a, will always be positive. Corrections for the gas concentrations will always be successful.

All proofs associated with **Scenario 7** can be applied to **Scenario 8** by interchanging the O_2 and the CO_2.

APPENDIX 2—CHAMBER PURGE

Assumptions:

1. Injection at a constant flow rate of gas mixture with a fixed composition in a constant volume chamber.
2. Gas within the chamber is well mixed so that the gas coming out of the chamber has the same composition as the gas within the chamber.

$x = x(t)$ = volumetric concentration of the gas in the chamber, a decimal
x_m = constant volumetric concentration of the gas in the injection mixture, a decimal
x_0 = initial volumetric concentration of the gas in the chamber, a decimal
V = volume of the chamber, m^3
D = Airflow in and out of the chamber, m^3/s

A balance gives:

$$V\frac{dx}{dt} = Dx_m - Dx$$

Reorganization of the equation gives:

$$\int \frac{dx}{(x_m - x)} = \int \frac{D}{V} dt$$

Integration gives:

$$-\ln(x_m - x) = \frac{D}{V}t + C_1$$

Where C_1 is an integration constant. The last equation can be reorganized as:

$$x_m - x = C_2 e^{\frac{-D}{V}t} \quad \text{where} \quad C_2 = e^{C_1}$$

With the initial condition the following equation is obtained:

$$x = x_m + (x_0 - x_m)e^{\frac{-D}{V}t}$$

NOTATION

x^0 = O_2 volumetric concentration before correction, a decimal
x^f = set point of O_2 volumetric concentration, a decimal
x = O_2 volumetric concentration at any time, a decimal
y^0 = CO_2 volumetric concentration before correction, a decimal
y^f = set point of CO_2 volumetric concentration, a decimal
y = CO_2 volumetric concentration at any time, a decimal
z^0 = N_2 volumetric concentration before correction, a decimal
z^f = N_2 volumetric concentration after correction, a decimal
t = time, s
t_1 = correction time of O_2, s
t_2 = correction time of CO_2, s
D_1 = injection flow rate of O_2, m^3/s
D_2 = injection flow rate of CO_2, m^3/s
D_3 = injection flow rate of N_2, m^3/s
V = volume of void space in the chamber, m^3

REFERENCES

1. Kader, A. A. 2002. *Postharvest technology of horticultural crops,* 3rd Edition. Oakland, CA: Agriculture and Natural Resources, University of California.
2. Thompson, A. K. 1998. Controlled atmosphere storage of fruits and vegetables. New York, NY: CAB International.
3. Goyette, B., C. Vigneault, N. R. Markarian and J. R. DeEll. "Design and implementation of an automated controlled atmosphere storage facility for research", Canadian Biosystems Engineering, Vol. 44, No. 3, 2002, pp. 35–40.
4. Markarian, N. R., C. Vigneault, Y. Gariepy and T. J. Rennie. "Computerized monitoring and control for a research controlled-atmosphere storage facility". Computers and Electronics in Agriculture. Vol. 39, 2003, pp. 23–37.
5. Raghavan, G. S. V., C. Vigneault, Y. Gariepy; N. R. Markarian and P. Alvo. 2005. Refrigerated and controlled/modified atmosphere storage. *Processing Fruits, Science and Technology,* 2nd Edition. Boca Raton, FL: CRC Press, pp. 23–52.
6. Mu, Y. 2005. A distributed control system for low pressure plant growth chambers, Ph.D. Dissertation, University of Florida.
7. Hublitz, I. 2006. Heat and mass transfer of low pressure Mars greenhouse : simulation and experimental analysis, Ph.D. Dissertation, University of Florida.
8. Bishop, D. 1990. Controlled atmosphere storage. Cold and Chilled Storage Technology, New York, NY: Van Nostrand Reinhold, pp. 66–98.
9. Jameson, J. 1981. The automated control of controlled atmosphere storage conditions. *Controlled Atmospheres for Storage and Transport of Perishable Agricultural Commodities, Proceedings of the Third National Controlled Atmosphere Research Conference,* Corvalis, OR: Oregon State University, Department of Horticulture, pp. 43–53.

Compression Strength Formulas for Bliss Cases and Wrap-around Boxes

CHANGFENG GE* and DANIEL GOODWIN
Rochester Institute of Technology, 78 Lomb Memorial Drive, Rochester, NY 14623-5604, USA

ABSTRACT: This paper is an updated development of a prior publication based on bliss case and wrap-around box styles. A study conducted at Rochester Institute of Technology (RIT) by Ge [1] determined that the McKee formula, an important functional performance indicator for top-to-bottom compression strength for regular slotted container (RSC), should be modified when applied to bliss cases and wrap-around boxes. In the study, corrugated box was evaluated as a combination of four panels, with the McKee formula applied to each panel to obtain the compression strengths and those values summed together.

Based on this methodology, this study developed compression strength equations for predicting the side-to-side compression strength for bliss cases and wraparound boxes. Box compression testing was performed for corrugated board boxes in two side directions to verify the compression formula. The observed variation between the predicted value and actual experimental data are matched.

The proposed modification methods to the McKee formula in this study leads to the conclusion that the McKee formula can be regarded as an universal compression strength formula in top-to-bottom and side-to-side for all corrugated box styles. This paper serves as a summary of the research into the compression strength prediction both in top-to-bottom and side-to-side for bliss cases and wrap-around boxes.

1. INTRODUCTION

CORRUGATED boxes are the most common transport packaging used in shipping the goods. There are many standard box styles such as slotted container, telescope boxes, folders, bliss boxes etc.[2]. Of these boxes, regular slotted container (RSC) is the most common box style used because of its cost effective and simple die-cut form. RSC also offers reasonable compression strength.

*Author to whom correspondence should be addressed. Email: cfgmet@rit.edu

1557-7244/10/03 155-13

Recently, the bliss case and wrap-around box styles are becoming the most utilized alternatives to the regular slotted container (RSC) due to the additional strength of the bliss case and the cost savings of the wrap-around box. The adaptability to automatic packaging process and the flexibility of the structure also make them the box type of choice with the growing trend of shelf ready and sustainable packaging.

Bliss case is six-sided container that consists of 3 pieces: a 'U' shape body, and two identical end-panels. The bliss-box is formed by a machine known simply as a bliss-former. These types of cases are more expensive than RSCs as they require expensive tooling to be purchased and a special machinery to assemble them. However the 3 piece box offers flexibility in assembling and printing. Different sizes of the box can be made by assembling the end panels and body die cut. The bliss case used in this study is 0601 under bliss case style [2].

The wrap-around box is formed tightly around a rigid product, such as a case of beer. The product is generally set on one of the center panels and a special machine wraps the blank around the product and glues the end panels to form a rigid container. This type of container resembles an RSC which is turned on its side; however the flutes of the board in this case run parallel to the length of the blank which allow for the flutes to remain parallel to the height of the container. Wrap-around boxes get most of their stacking strength from the product inside since they are formed tightly around a product with uniform surfaces generally. The wrap-around box used in this study is 0406 under the folder style category [2].

The box compression predicting formula developed by R.C. McKee and has been effectively used by the packaging industry for many years due to its simple format. The formula is, however, restricted to Regular

Figure 1. *Three styles of the corrugated boxes (drawings are courtesy of Fibre Box Association) [2].*

Slotted Containers (RSC). Since then, the formula has not been kept up to date as more corrugated box styles have been used, such as bliss-cases and wrap-around boxes.

The purpose of the paper is to summarize the development in predicting the top-to-bottom compression strength of bliss cases and wrap around boxes and develop the side-to-side compression strength prediction for bliss cases and wrap-around boxes.

2. BACKGROUND OF COMPRESSION STRENGTH STUDIES

The top-to bottom compression strength is one of the most important functional performance indicators of the corrugated board box. In 1963, R.C. McKee developed the box compression predicting formula as follows:

$$P\ (\text{lb}) = 5.87 \times ECT \times \sqrt{T \times ID} \tag{1}$$

ECT is the edge crush test value (lb/in); *T* is the board thickness (in); and *ID* is the internal perimeter (2Length + 2Width) of the box (in).

The equation uses the *ECT* value, board thickness, and perimeter of the box to calculate the top-to-bottom compression strength. The application assumptions made by the McKee formula are (1) it is applied only to the RSC style boxes; (2) it is applied to boxes where the length is less than three times the width; (3) it is applied to boxes where the perimeter is less than seven times the box depth.

Over the years, very few researchers have made an effort to modify the McKee formula to accommodate other box styles. One exception was postulated by Joseph J. Balteka and Carl N. Smith of the Institute of Paper Science and Technology. In 1993, Baltelka and Smith proposed the following modification to the McKee formula based on McKee formula before simplification:

McKee formula before simplification by McKee:

$$P = 2.028 \times ([(ECT)]^{0.746} \times (Dx \times Dy)^{0.127} \times (ID)^{0.492} \tag{2}$$

Proposed Modification by Balteka and Smith:

$$P = 1.014 \times ([(ECT)]^{0.746} \times (Dx \times Dy)^{0.127} \times (\Sigma W)^{0.492} \times 1.593 \times (d))^{-0.236} \tag{3}$$

Where P is compression strength (lb), Dx and Dy are the flexural stiffness (lb-in), W is the width of each panel (in) and d is the depth of the box (in).

This modified formula expands the potential application spectrum of the original McKee formula by including the variable for flexural stiffness, Dx and Dy. However, for the purposes of practicality and industry adoption, McKee opts for a simpler albeit more application-limited formula. Determining the value of flexural stiffness, Dx and Dy, requires specific measurement equipment that is not readily available at every corrugated board company. As a matter of pragmatic business practice, companies prefer having a one step top-to-bottom compression test rather than taking two steps determining compression strength by first measuring Dx and Dy and then, using the more complex formula.

There were few publications on how to estimate the side-to-side compression strength of a regular slotted container, Maltenfort [6] developed the following side-to-side compression prediction formula for a horizontal flute container based on Mc Kee formula. This was the formula for horizontal flute boxes stacked on their sides.

$$P = 3.57 \times ECT \times \sqrt{T \times ID} \times \left(1 + \frac{W}{L}\right) \tag{4}$$

Where ID is the perimeter < 52 in; W is the width of the box ≥ 10in; L is the length of the box. ECT is edge crush test value (in vertical flute).

This above formula expands the application of the original McKee formula to a different box style by including a coefficient on effect of the gap where the two side panels meet. Since then, no similar research was carried out in this area as the horizontal flute container are no longer in the market. However, the gap panel coefficient 3.57 derived from Maltenfort's research is valuable input for evaluating the compression strength of bliss cases and wrap-around boxes.

3. TOP-TO-BOTTOM COMPRESSION STRENGTH FOR BLISS CASES AND WRAP-AROUND BOXES

Research at RIT [1] on measuring the compression strength of the bliss cases and wrap-around boxes led to the development of following equations, based on modifications to the simplified McKee formula, the top-to bottom compression strength for the two box styles could be predicted as follows:

Top-to-bottom Compression Strength Prediction Formula for Bliss Case

$$F(lb) = 5.87 \times ECT \times \sqrt{TB \times ID} \tag{5}$$

Where:

$$ID = 2L + 2W \times \text{width of the manufacturing joint (in)}$$

$$TB = T + \frac{3 \times \text{width of the manufacturing joint}}{2L + 2W} \times T \text{ (in)}$$

T is the board thickness (in)

The compression strength formula for wrap-around box where the width panel w is defined as the panel having horizontal flute glued with the vertical flute.

Top-to-bottom Compression Strength Prediction Formula for Wrap-around Box

$$P(lb) = \frac{2L}{2L + 2W} + 5.87 \times ECT \times \sqrt{T \times ID} + \frac{2W}{2L + 2W} \times 3.57 \times ECT \times \sqrt{T \times ID} \tag{6}$$

Where:

$$ID = 2L + 2W \text{ (in)}$$

T is the board thickness (in)

In Equation (6), wrap-around box is regarded as a combination of four panels, with the McKee formula applied to each panel to obtain the compression strengths and those values summed together. The first part

$$\frac{2L}{2L + 2W} \times 5.87 \times ECT \times \sqrt{T \times ID}$$

represents the strength of the two panels with vertical flute, the part

$$\frac{2W}{2L + 2W} \times 3.57 \times ECT \times \sqrt{T \times ID}$$

represents the two side panels with gap in the middle.

According to the above formulas, a bliss case, a wrap-around box and

Table 1. *Comparison of the Tested Results and Predicted Results.*

	Top-to-bottom Compression Strength (kg)		
Evaluation Method	**Bliss Case**	**Wrap-around Box**	**RSC**
Tested results	350.66	261.27	330.24
Predicted results	298.61	219.53	273.02
Difference	17.42%	19%	20%

a RSC, with an internal dimension (*ID*) of 32.48 × 32.48 × 20.32 cm, thickness *T* of 0.4064 cm (0.16 in), and ECT of 17 N/cm (37 lbs/in) had the top-to-bottom strength of 298.62 kg, 219.53 kg and 273.02 kg respectively.

Experimental comparisons based on 18 samples were made to compare the compression strength between predicted value and the tested value. The comparison results were summarized in Table 1:

The finding from Table 1 showed that the difference between the predicted and tested value among these three box styles was minimal. That result indicated that if the McKee formula had proven to be a solid indicator of top-to-bottom compression strength for an RSC, then, the developed formula for bliss case and wrap-around box would also result in good predictions of top-to-bottom compression strength for bliss case and wrap-around box too.

4. SIDE-TO-SIDE COMPRESSION STRENGTH FOR BLISS CASES AND WRAP-AROUND BOXES

Side-to-side compression strength of a shipping box is an important strength indicator that has not been meaningfully explored. Two transportation and distribution modes have caused shipping box damage: (1) the side area of the corrugated box is used as a support panel in a truck and (2) unitized load impact each other between the palletized units in horizontal directions during the transportation. The former is common in transporting the product intermixed with various sized packaging boxes from the warehouse environment to the retailer.

4.1 Edge Crush Test Value

When panels with horizontal flute of a corrugated box act as support panels, the side-to-side box compression can not be predicted using the

McKee formula. Because the *ECT* value is derived by compressing the corrugated board in a vertical flute direction whereas in the case of side-to-side compression, the box panels are compressed in a direction that is perpendicular to the flute direction. In order to predict the side-to-side compression strength of a box using McKee formula, two *ECT* values are proposed to apply in the McKee formula: the *ECT* value in the vertical flute (ECT_v) that is commonly understood as *ECT* value and the *ECT* value in the horizontal flute (ECT_h).

Ten (10) of 5.08 cm × 5.08 cm samples were tested to obtain the both ECT values in the edge crush tester based on TAPPI standard TIP0304-09. Interestingly, the ECT_v value was two times the ECT h. value. The following table summarizes the measured *ECT* values according to TAPPI standard TIP0304-09 in both the horizontal and vertical direction.

4.2 Compression Strength for Box and Panels

A corrugated board box consists of four side panels regardless of the box style. The total side-to-side strength of a corrugated box is the sum of the strengths of the four individual side panels. The foundation of the McKee formula was based on the assumption that the box consisted of four side panels. The individual panel compression strengths were summed for total box strength. Therefore, the *ECT* value in the McKee formula is suggested to depend on the flute direction of the panel. When a corrugated board with the horizontal flute acts as a vertical panel to support the box, the *ECT* value in horizontal flute direction (ECT_h) value

Table 2. *Edge Crush Test Value in Vertical and Horizontal Flute Tested Under 23°C and 50%RH.*

Samples	ECT_v N/cm (lbs/in)	ECT_h N/cm (lbs/in)
1	63 (36)	32 (18)
2	67 (38)	33 (19)
3	65 (37)	30 (17)
4	58 (33)	35 (20)
5	63 (36)	26 (15)
6	58 (33)	30 (17)
7	54 (31)	35 (20)
8	63 (36)	30 (17)
9	68 (39)	35 (20)
10	67 (38)	30 (17)
Averaged	63 (36)	32 (18)

should be used in the formula. When two flap panels meet in the middle of a corrugated box, the coefficient of 3.57 [6] is suggested to be placed in the McKee formula to predict the compression strength.

A series of detailed side middle-cross section views for a closed box are illustrated below, clarifying the views of the four panels with vertical flute and horizontal flute. The views serve as the basic configuration to develop the modified McKee formula.

If a bliss case has a dimension of $L \times W \times H$, with an ECT_v and ECT_h, the estimated side-to-side compression strength P could be predicted as follows:

Side-to-side Strength *P* of a Bliss Case on the Length Side (Figure 2)

$$P\ (\text{lb}) = \frac{2H}{2L+2H} \times 5.87 \times ECT_h \times \sqrt{T \times ID} + \frac{L}{2L+2H} \times 3.57 \times ECT_v \times \sqrt{T \times ID} + \frac{L}{2L+2H} \times 5.87 \times ECT_v \times \sqrt{T \times ID} \quad (7)$$

Where: T is the board thickness (in); $ID = 2L + 2H$ (in).

Side-to-side Strength *P* of a Bliss Case on the Width Side (Figure 3)

$$P\ (\text{lb}) = \frac{2H}{2W+2H} \times 5.87 \times ECT_h \times \sqrt{T \times ID} + \frac{W}{2W+2H} \times 5.87 \times ECT_h \times \sqrt{T \times ID} + \frac{W}{2W+2H} \times 3.57 \times ECT_h \times \sqrt{T \times ID} \quad (8)$$

Where T is the thickness of the board (in); $ID = 2W + 2H$ (in).

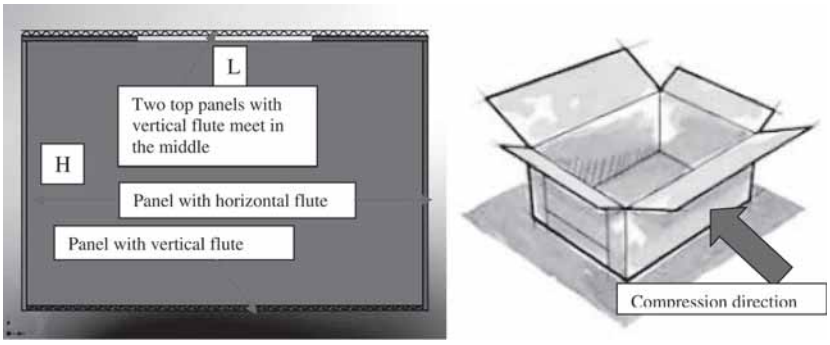

Figure 2. *Cross section view of a closed bliss case on the length side.*

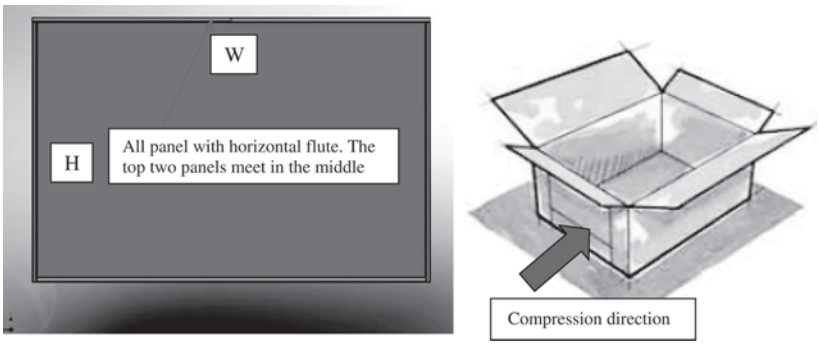

Figure 3. *Cross section view of a closed bliss case on the width side.*

Similarly, if a warp-around box has a dimension of $L \times W \times H$, with an ECT_v and ECT_h, the estimated side-to-side compression strength P can be described in the following formula:

Side-to-side Strength *P* of a Wrap-around Box on the Length Side (Figure 4)

$$P\ (\text{lb}) = \frac{2L}{2L+2H} \times 5.87 \times ECT_v \times \sqrt{T \times ID} + \frac{2H}{2L+2H} \times 3.57 \times ECT_v \times \sqrt{T \times ID} \quad (9)$$

Where T is the board thickness (in); $ID = 2L + 2H$ (in).

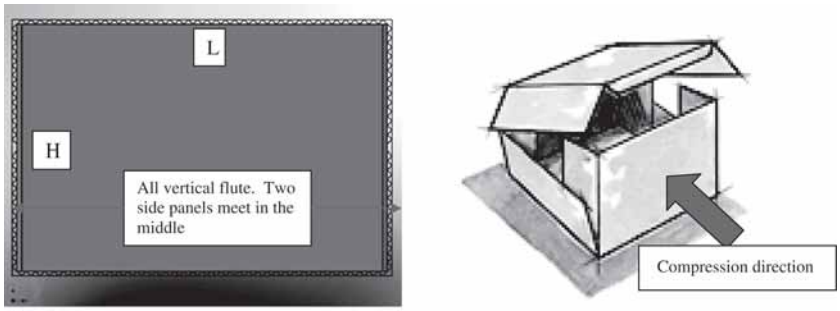

Figure 4. *Cross section view of a closed wrap-around box on the length side.*

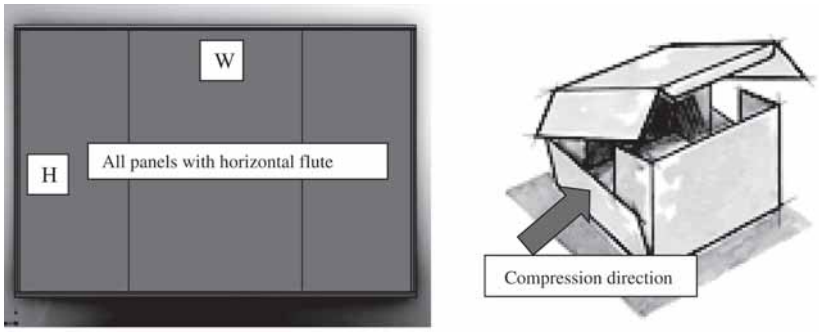

Figure 5. *Cross section view of a closed wrap-around box on the width side.*

Side-to-side Strength *P* of a Wrap-around Box on the Width Side (Figure 5)

$$P\ (\text{lb}) = 5.87 \times ECT_h \times \sqrt{T \times ID} \tag{10}$$

Where T is the board thickness (in); $ID = 2W + 2H$ (in).

According to the above formulas, a bliss case and a wrap-around box, with an internal dimension (ID) of 32.48 × 32.48 × 20.32 (cm), thickness T of 0.4064 cm (0.16 in), ECT_v of 63N/cm (36 lbs/in) and ECT_h of 32 N/cm (18 lbs/in), had the following side-to-side compression strength.

5. SIDE-TO-SIDE BOX COMPRESSION TESTING

The two groups of samples using 14.52 kg (32 lb) C-flute corrugated board were designed using the ArtiosCAD software based on the FEFCO 0601(bliss case) and 0406 (wrap-around box).

The final drawings of 0601 and 0406 were modified from ArtiosCAD's database to reflect the common practice in the industry.

Table 3. *Predicted Side-to-side Compression Strength for Bliss Cases and Wrap-around Boxes.*

Box Style	Side Strength on Long Side (kg)	Side Strength on Width Side (kg)
Bliss case	165	107
Wrap-around box	205	121

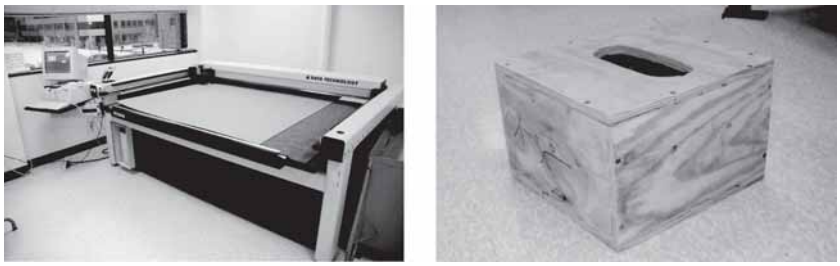

Figure 6. *Cutting table (left); Wood box as internal product for setting up the box (right).*

Following the virtual creation of the boxes, an HPGL file was exported to the Data Technology cutting table to cut the samples out.

Each group consists of 5 samples with an internal dimension (*ID*) of 30.48 cm (*L*) × 30.48 cm × 20.32 cm(*H*). In order to ensure the consistency, a wooden box with an outer dimension (*OD*) of 32.48cm × 32.48 cm × 20.32 cm was used to act as internal product and a fixture for setting up the box manually. All boxes were assembled using a hot-melt glue gun on all manufacturing joints.

ASTM D 642 standards were followed while compression testing. The Lansmont compression tester was used to conduct the testing. It had a 22.68 kg (50 lb). preload. The test velocity was 2.54 cm/min. Auto sample and auto log on test completions were turned on. The compression machine automatically stopped the test when a −1.27 cm deflection of the box occurred or a −10% of maximum yield appeared during the compression test.

Following table summarizes the experimental obtained compression strength *P* and the associated deflection *S* for each type of box in two direction.

Table 4. *Tested Compression Strength of Bliss Cases.*

	Bliss Case (Width)			Bliss Case (Length)	
Samples	Peak Force (kg)	Deflection (cm)	Samples	Peak Force (kg)	Deflection (cm)
1	123.33	0.36	1	151.01	0.48
2	145.42	0.28	2	106.28	0.53
3	75.62	0.97	3	328.30	0.48
4	118.16	0.48	4	148.92	0.28
5	104.69	0.48	5	114.35	0.23
Average	113.45	0.51	Average	128.26	0.41

Table 5. *Tested Compression Strength of Wrap-around Boxes.*

	Wrap-around (Length)			Wrap-around (Width)	
Samples	Peak Force (kg)	Deflection (cm)	Samples	Peak Force (kg)	Deflection (cm)
1	154.27	0.66	1	94.53	0.762
2	173.96	0.43	2	85.46	0.46
3	192.60	0.79	3	85.73	0.94
4	167.70	0.69	4	78.93	0.30
5	90.58	0.25	5	101.56	1.27
Average	155.82	0.56	Average	89.24	0.74

6. COMPARISON ANALYSIS

From the above table, the prediction value and actual testing value had a difference ranging from 5.6% to 22.42 % for the bliss case. The difference for the wrap-around box was relatively large variation ranging from 23.73% to 26.22%. The lower than expected experimental values for wrap-around box were largely contributed to the failure of the hot glue adhesive causing separation of the manufacturing joint during compression testing.

Both the bliss case and the wrap-around box have a higher side-to-side compression strengths in the length direction compared to the width direction because all four panels or two panels are in the vertical flute direction. The relative lower compression strength in the side-to-side is a result of the four support panels having a horizontal flute profile.

7. CONCLUSION

When comparing the predicted and tested results, the predicted values and experimental values reasonably matched in the prior research and current study. Both the tested and calculated compression strength values showed that the bliss case has the highest compression strength, followed by the RSC and wrap-around box in top-to-bottom compression strength. The wrap-around box has a relatively higher side-to side compression strength in length direction compared to the width direction. The bliss case has a relatively smaller difference in the side-to-side compression strength between the length direction and width direction.

This paper and previous research at RIT propose a useful concept regarding prediction of compression strength of a corrugated box. Corru-

Table 6. *Comparison of Compression Strength Between Predicted and Experimental Obtained Results.*

	CompressionStrength in Length Direction (kg)			Compression Strength in Width Direction (kg)		
Box style	**Predicted**	**Experiment**	**Difference**	**Predicted**	**Experiment**	**Difference**
Bliss case	165	128	22.42%	107	113	5.50%
Wrap-around box	205	156	23.73%	121	89	26.20%

gated box is evaluated in fact as a combination of four panels. The McKee formula is applied to each panel for an RSC to obtain the compression strengths and those values are summed together as box compression strength. Because the four (4) panels of a RSC box has the identical vertical flute direction, McKee formula is able to be simplified as it is. When applied to a box style different from an RSC (the four panels of the box have different flute direction) to predict the top-to-bottom compression strength, McKee formula is suggested to have the compression strengths of each panel be measured and the values are added together as the compression strength of the entire box. This method leads to the conclusion that McKee's formula can apply to all corrugated box styles.

Further work is required to engage box plants and/or manufacturers to conduct the box compression testing for the commercially produced bliss box and wrap-around box styles to verify these proposed formulas and findings. The coefficients in the formulas could be fine tuned in accordance to the recent industry practice.

REFERENCES

1. Changfeng Ge, Thomas Kausch and Daniel Goodwin, An Experimental Comparison of Compression Strength: Regular Slotted Containers, Bliss Cases and Wrap-around Boxes, IAPRI World conference on packaging, 2008, Bangkok.
2. Fibre Box Association, Fibre Box Handbook, 2003. www.fibrebox.org
3. R.C. McKee, J.W. Gander and J.R. Wachuta, Compression Strength Formula for corrugated board paper board packaging, P 149û159, August 1963
4. J.J. Batelka and C.N. Smith, Packaging Compression Model , Project report to the American Forest and Paper Association, 1993
5. Thomas J.Urbanik, Finite Element Corroboration of Buckling Phenomena Observed in Corrugated Box, Wood and Fiber Science, July (2003) Vol 35(3)
6. George G. Maltenfort, Estimating Side-to-Side Compression of Horizontal Flute Containersö, page 182–186, Performance and Evaluation of Shipping Containers, 1989 by Jelmar Publishing Co.Inc.

Oxygen Permeability of Semi-rigid Polymers Coated with Polyacrilic Acid Filled Polymer-clay Nanocompsite Coatings Produced Under Different pH Conditions

JINWOO KWAK[1], SUNGWAN JEON[2], SIOBAN MATTHEWS[3], BRUCE WELT[2,*] and CHARLES BEATTY[1]

[1]*Dept. of Material Science and Engineering, University of Florida, Gainesville, FL 32608*

[2]*Packaging Science Program, Agricultural and Biological Engineering Department, University of Florida, Gainesville, FL 32608*

[3]*SCF Processing Ltd, Drogheda, Ireland*

ABSTRACT: The purpose of this work was to develop a high barrier, polymer-clay nanocomposite coating. An approach was developed to create a unique collapsed "house-of-cards" structure using specially treated oligomers to further fill structural voids of the structure. Laponite JS and negatively charged poly(acrylic acid) (PAA) oligomers were used to create stratified microstructures through face-to-face attachment of oligomer to clay platelets. PAA in basic condition played a role as a linkage molecule to realize edge-to-edge contact between clay platelets. Overall oxygen transmission rates were reduced by a factor of 10 to about 10 cc/m^2/day for samples produced at ph 6. A significant amount of cracks on the surface were observed by scanning electron microscopy when coated with solutions prepared at pH 2 and 4. These cracks resulted in significant loss of coating barrier properties suggesting pH 6 as the most suitable condition for production of this barrier coating.

INTRODUCTION

PROPERTIES of polymer clay nanocomposite (PCN) materials can be enhanced by altering the characteristics of filler particles due to competitive interactions between attractive forces of polymer chains and silicate layers, and electrostatic forces between silicate layers. One

*Author to whom correspondence should be addressed. Email: bwelt@ufl.edu

1557-7244/10/03 169-20

of three microstructures of silicate platelets in a polymer matrix (phase-separated, intercalated, and exfoliated) usually dominates when a composite is formed. Each microstructure can be tailored by adjusting a variety of factors such as silicate particle types [1,4,5], volume fraction of particles [9,10,15], and the processing techniques used [3,5,6,8].

The aim of this study was to optimize oxygen barrier properties of PCN films by designing and engineering the microstructure of silicate particles. According to the detour models of permeability [2], parallel platelets are required to be perpendicular to the permeation direction to achieve superior barrier materials. However, in real nanocomposite systems, crystallization characteristics of the polymer [19,20], degree of dispersion/exfoliation [12,15,18] and orientation of clay particles [12,18,21] will hinder ideal barrier routes. To minimize these possible hindrance factors and extend attainable detour length in composite materials, a dense stratification of silicate platelets using a polymer as a binder material to be attached to the edges of platelets was devised.

The silicate particles used in this study were Laponite JS. The concentration of sodium ions over the whole surface of the Laponite JS platelets in the intergallery regions was constant prior to addition of platelets into water. Initially, when clay platelets were added to the water, the clay powder formed the aggregated particle stacks. These stacks were separated and swollen by the hydration of sodium ions (Figure 1).

Hydrated sodium ions distributed in the intergallery are affected by two forces; electrostatic attraction with a negatively charged platelet surface and osmotic pressure caused by differences in chemical potential between intergallery phase and aqueous phase. Osmotic pressure applied to sodium ions at crystal edges should be stronger than at the central region. Furthermore, when two crystals approach, tmutual positive charges repel each other. Therefore, hydration of sodium ions and mutual repulsive forces open intergallery regions, lowering osmotic pressure. As a result, sodium ions at platelet centers tend to be attracted more to surfaces than edges. Therefore, this should lead to concentration gradients of sodium ions over platelet surfaces [Figure 2(a)].

To halt further diffusion of sodium ions and reach a stable equilibrium, addition of polar compounds was required. Addition of polar compounds should result in weaker positive ions being attracted to negative surface charges of adjacent particles forming a unique structure [Figure 2(b) and (c)]. As a result of a series of these successive interactions in the system, a structure that we refer to as a ‘house of cards’ (HOC) consist-

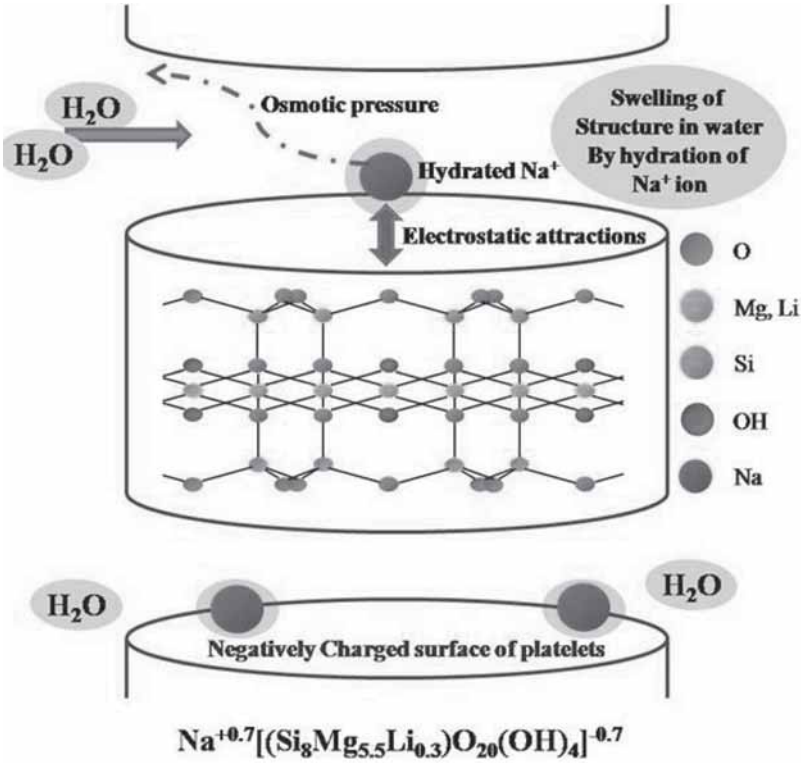

Figure 1. *Structure of silicate layers, Laponite JS when dispersed in water phase.*

ing of weak ionic bonds is formed. Further, this HOC structure was expected to collapse when the system was dehydrated. To maintain this densely stratified structure and to fill interstitial microvoids, a polymer capable of attaching to neighboring central surfaces was used. Ogoshi and Chujo [22] proposed that optically transparent organic-inorganic polymer hybrids with anionic polymers could be prepared by controlling pH in an aqueous solution. They also reported that the structure of the anionic polymer, polyacrylic acid (PAA), could be controlled by varying pH due to charge repulsion between polymer chains. Gudeman and Peppas [23] also found that the swelling ratio of poly(vinyl alcohol) (PVA)/PAA interpenetrating network can be adjusted by varying pH in an aqueous solution.

In this study, oligomeric PAA was used as the HOC void filling polymer. Anionic PAA can be prepared by dissolving PAA chains in a basic solution. As a result, PAA chains are extended by mutual electric repul-

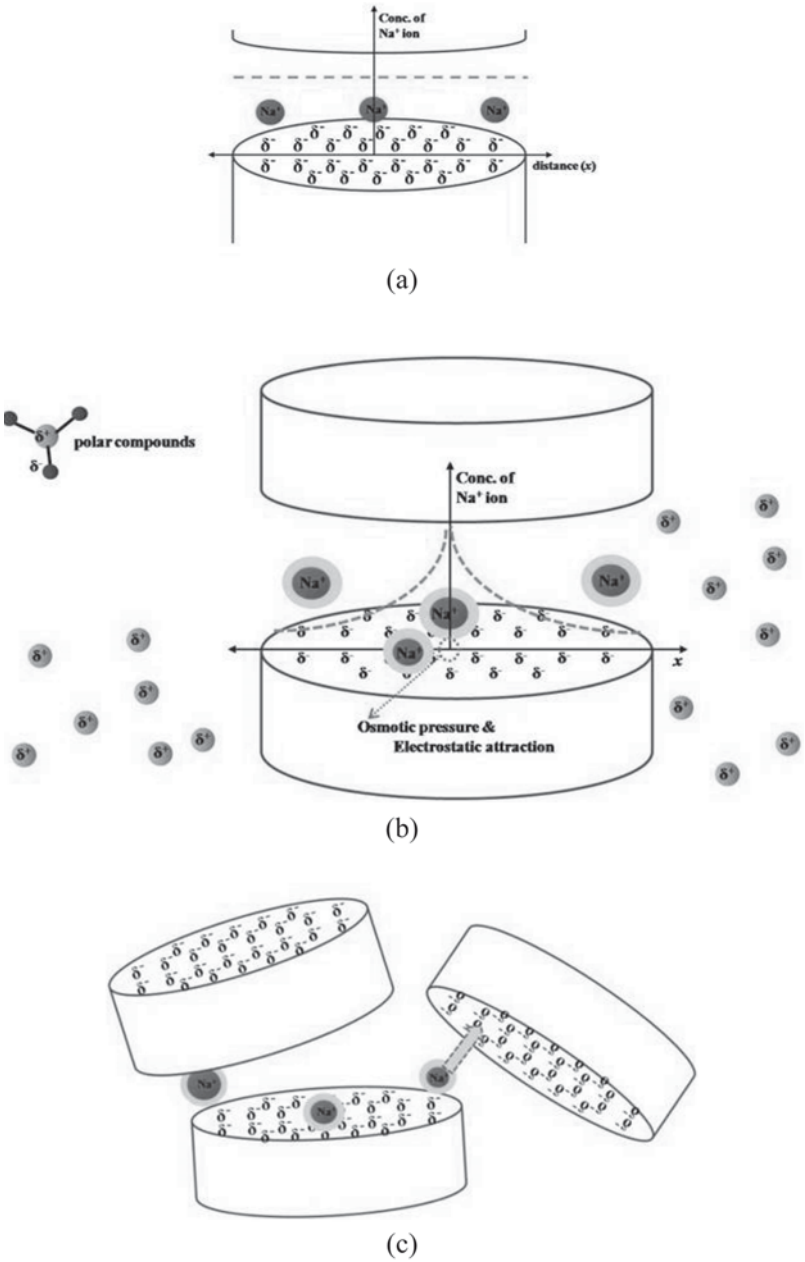

Figure 2. *Schematic mechanism of 'a house of cards' structure (a) initial stage as a powder state, (b) the formation of concentration gradient of sodium ions in the intergallery regions and the addition of polar compounds and (c) the formation of 'a house of cards" structure.*

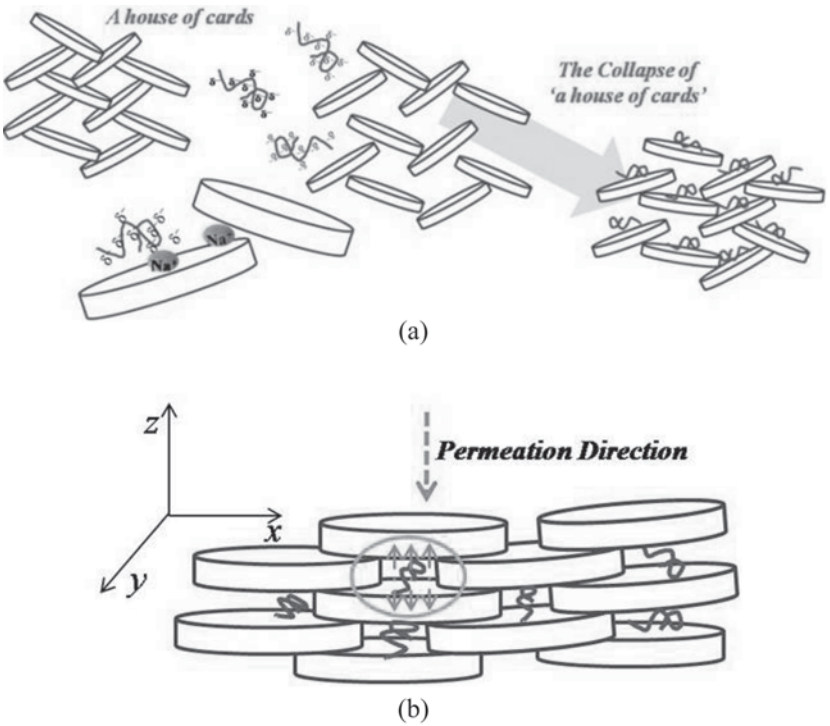

Figure 3. *(a) Schematic mechanism of 'a house of cards' structure through the diffusion of oligomeric anionic PAA chains into a clay structure and (b) expected ideal barrier structure.*

sive forces between chains as the side chains are negatively charged (COO^-). These PAA chains should be short enough to fill the microvoids. The driving force of PAA chains into microvoids is electric attraction [Figure 3(a)].

PAA chains are attracted to centers of platelets as the positive ions at edges are relatively weak and already bonded with adjacent crystals forming HOC structures. Weak shear forces helped the short PAA chains to diffuse into the structure and, with time, reorientation and relaxation of clay platelets removed shear forces. The drying process and appropriate degree of external pressure led to dense stratified clay structures filled with PAA chains. Therefore, anionic PAA attaches two crystals by electrostatic force and the ideal barrier structure may be obtained by forming densely stratified structure [Figure 3(b)]. In this study, the microstructure of clay platelets for better barrier properties was devised based on the concept suggested by Ebina [13] and Tetsuka [14]. Effects

of pH on microstructure of clay particles and barrier properties of resulting composite-coated films was evaluated for barrier performance and structural characterization.

EXPERIMENTS

Preparation of Polymer Clay Nanocomposite Solutions at Various pHs

HOC structure was identified by investigating the microstructure of clay aerogel. At first, a clay hydrogel was prepared from 15 wt% clay aqueous solution with ammonium chloride and sodium tetraborate as additives after aging for 24 hours. A clay hydrogel was frozen in 2L glass lyophilization shells at 173K (−100°C) and a frozen clay hydrogel was sublimed using a labconco Freeze Dryer 8. Half-filled shells were rotated at 30 rpm at a temperature of −80°C until frozen and the ice from frozen shells was then evacuated for 36 hrs.

To prepare composite coating solution, first of all, low molecular weight PAA (Degree of Polymerization (DP) of 25) was dissolved in distilled water and the pH of the mixture was controlled using aqueous HCl (1 M) or NaOH (1 M) solution. PAA chains under three different conditions (acidic, basic and intermediate condition) were prepared to compare effects of pH on the filling void and stratifying clay platelets. An amount of Laponite JS based on weight ratio of clay to PAA in the final dried film was added into deionized water gradually to prevent aggregation. Samples were premixed for 1–2 minutes with a magnetic stir-

Table 1. *Specific Conditions for the Preparation of Each Specimen.*

			PAA	
#	Sample Name	Clay (wt%)	pH	Ratio (by weight)
1	C5PA91AS	5	2	9:1
2	C5PA91IS	5	4	9:1
3	C5PA91BS	5	6	9:1
4	C5PA73AS	5	2	7:3
5	C5PA73IS	5	4	7:3
6	C5PA73BS	5	6	7:3
7	C5PA55AS	5	2	5:5
8	C5PA55IS5	5	4	5:5
9	C5PA55BS	5	6	5:5

rer. Polar compound, ammonium chloride (NH_4Cl) buffer solution, at 1 wt% (according to the amount of clay used) was added to solution to lower osmotic pressure in the intergallery. Prepared PAA stock solution was added into the clay mixture and mixed gently for 1 hour with a magnetic stirrer. A prepared mixture of water, clay, polar compound, and PAA was degassed in vacuum to minimize structural defects by removing remaining flocculated or aggregated clay impurities. Specific conditions for preparation of nanocomposite solutions are listed in Table 1.

Coating Samples After Atmospheric Pressure Plasma Treatment

Optimumal conditions for atmospheric pressure plasma (APP) treatment were chosen based on the previous results [7]. These conditions were 18 l/min of nitrogen gas flow rate, 20 mm of working distance, and 4 treatment times. Composite solutions were coated on isotactic (i-) polypropylene (PP) film after APP treatment to enhance adhesion. Surfaces of rigid PP were spin coated (Laurell WS-400B-6NPP/LITE, Laurell Technologies Co., North Wales, PA) with 20g coating solution at fixed spin-coating parameters involving a two-step process. First step was 500 rpm for 1.5 min. Second step was 700 rpm for 30s. Samples were dried at ambient temperature in a vacuum desiccator.

Characterizations and Analysis

Chain conformations of anionic PAA in composite material were identified by Diffuse Reflectance Infrared Fourier Transform (DRIFT) Spectroscopy (Thermo Electron Magna 760, Thermo Scientific Inc., MA). The structure of the clay film was characterized by WAXRD (Philips XRD APD 3720 powder diffractometer, Philips Electronics, Mahwah, NJ). The change in spacing was measured using an X-ray diffractometer with a Cu anode (CuKα radiation λ = 1.54056 Å) with a wide range scanning angle. Clay and clay composite powder were mounted on a sample holder with a large cavity; a smooth surface was obtained by pressing particles with a glass plate. A clay composite sample prepared by rod coating on a silicon wafer was compared with the composite powder to investigate effects of coating shear direction on orientation of clay platelets. X-ray diffraction patterns were obtained at the small angle range from 2° to 10° to investigate effects of polymer

loadings on microstructures of clay platelets using WAXRD (Philips MRD X'Pert System, Philips Electronics, Mahwah, NJ) with a rotation anode and CuKα radiation. PCN-coated PP specimens were able to be used directly without a sample holder.

In order to analyze the morphological characteristics of clay aerogel and surfaces of composite films, those samples were sputter coated with gold-palladium alloy (Au-Pd) and observed using SEM (JSM-6400, Jeol Ltd., Tokyo, Japan). TEM (TEM-200CX, Jeol Ltd., Tokyo, Japan) micrographs of clay film showed microstructure of clay platelets. TEM was operated at an accelerating voltage of 200 kV. The dispersion liquid was dropped directly on a copper grid supported with a collodion membrane. Oxygen transmission rate (OTR) values of coated specimens were measured in accordance with the procedure described in ASTM D-3985 using a Model OX-TRAN 2/20MH (Mocon Corporation, Minneapolis, MN) to investigate barrier properties.

RESULTS AND DISCUSSION

House of Cards Structure

A 'hhouse of cards' structure of Laponite JS clay powder in the aqueous solution was identified by investigation of the microstructure of clay aerogel. Figure 4 shows the changes in morphology from the clay powder to clay aerogel. As shown in SEM micrographs [Figure 4(a) and (b)], the structure of nanoclay powder as received was a randomly stacked aggregate while the clay aerogel [Figure 4(c) and (d)] showed regular microchannels in the range of 5–20 μm in the bulk. This structure is representation of a house of cards formation mechanism (Figure 2 and 3). Morphological features and formation of house of cards structure have been reported by several researchers [11,16,17,24].

Corresponding TEM micrographs are shown in Figure 5. Aggregated platelets clumped together due to van der Waals attraction in dry conditions showing large dark spots containing several dark lines representing edge-standing platelets. HOC structure predicts platelets arranged in tilted, edge-standing, and paralleled platelets to the surface.

Effects of pH on the Clay Platelet Microstructure

It has already been reported that PAA may be modified via pH in

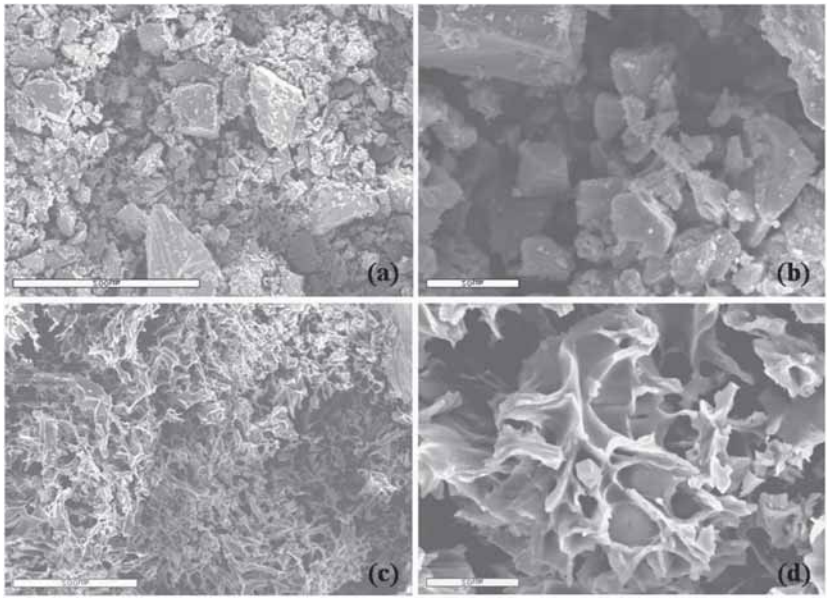

Figure 4. *SEM micrographs of (a, b) Laponite JS clay powder and (c, d) corresponding clay aerogel.*

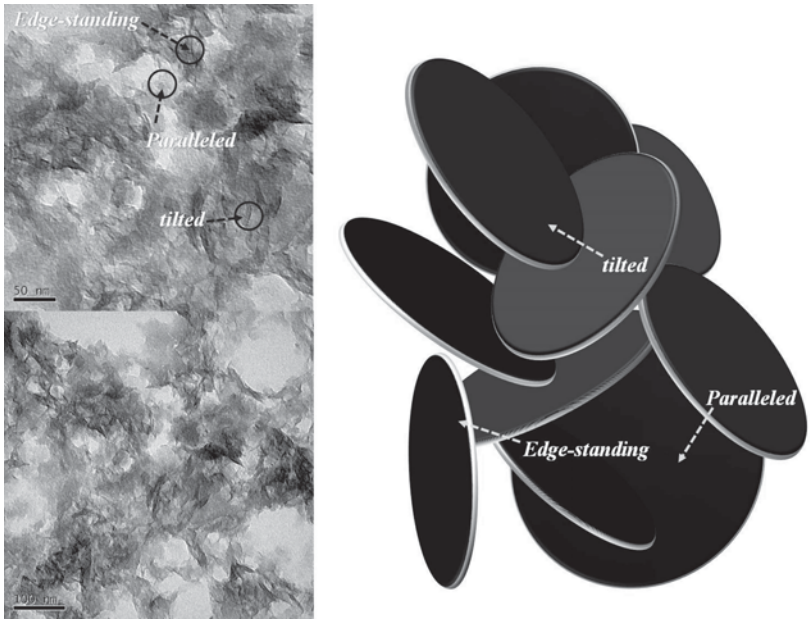

Figure 5. *TEM micrographs of clay aerogel consisting of three structural features, edge-standing, tilted and paralleled as indicated as arrows.*

aqueous solution [23]. PAA chains under basic condition can be expanded by electrical repulsive forces resulting in dissociation of ionic groups. Therefore, it was necessary to estimate ranges of molecular weights of PAA to best fit interstitial voids of the HOC structure. It was assumed that PAA chains were fully extended under basic conditions due to electric repulsion among adjacent carboxylic anions. End-to-end distance <R> (<R> = nl, where n is the number of repeat unit and l is the bond length) was used to estimate an approximate molecular weight of PAA that would be able to diffuse into HOC voids. Average surface diameter of Laponite JS is 55 nm and bond length of C–C is 0.15 nm and therefore 'n' should be in the range of 1 and 336, which means that low molecular weight or oligomer of PAA was required.

The chain conformations of anionic PAA in composite material were identified by DRIFT Spectroscopy as shown in Figure 6. The peaks at 1550 cm^{-1} and 1710 cm^{-1} are for C=O stretching vibration of the carboxylic anion (–COO–) and carboxylic acid group (–COOH), respectively. In the case of PAA under basic conditions, relatively higher peaks at 1550 cm^{-1} were detected, while the much higher peak at 1710 cm^{-1} for PAA under acidic condition was observed. Under acidic condi-

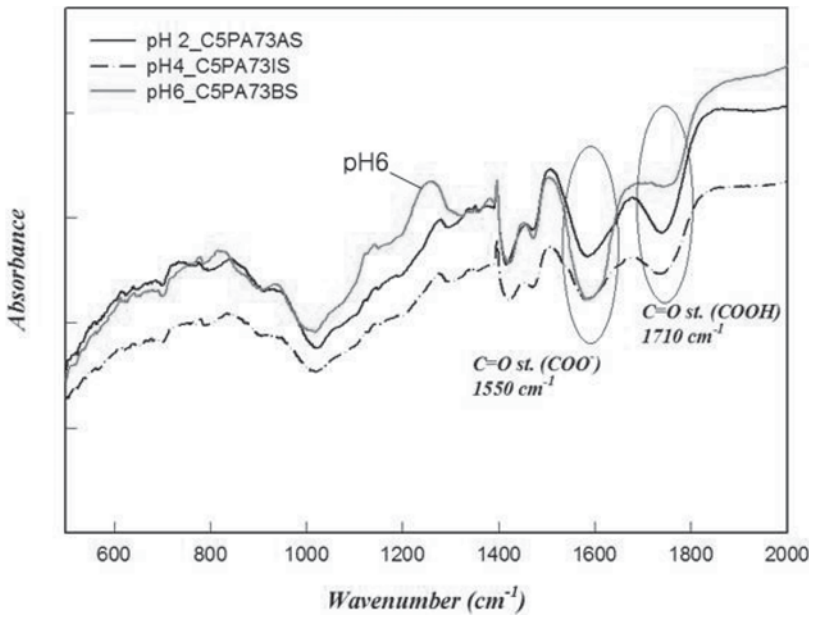

Figure 6. *DRIFT results of composite samples of C5PA73 prepared at pH 2, 4, and 6.*

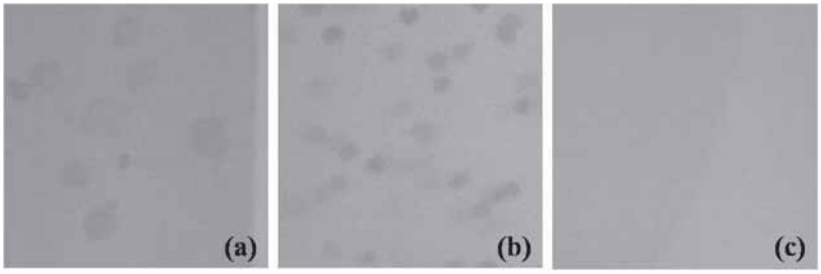

Figure 7. *Photographs of the states of composite solutions prepared under different pH conditions; (a) pH 2 (b) pH 4, and (c) pH 6 after 3 weeks storage.*

tions, short PAA chains become entangled together rather than extending, showing a critical concentration which will not allow PAA chains to diffuse as desired. This appears to have been confirmed by experimental evidence. Aggregated white small particles were dispersed in a composite gel as shown in Figure 7 for the case of samples prepared under acidic and isoelectric point (IEP) conditions after 3 weeks storage. These particles can be formed by two possible reactions. The first possibility is salt extraction caused by sodium cation diffusion from intergallery regions and dissociated chlorine anions from added ammonium chloride. The other possibility is phase separation of entangled PAA chains due to the higher intra- and intermolecular hydrogen bonding in acidic conditions.

To examine which reaction occurred in the system at various pH levels, SEM samples were prepared by drying gel-like samples on a glass slide at 70°C for 1 day. The white particles were mounted on SEM sample holders using sharp tweezers. Some small residual dry clay particles were shown adjacent to these larger particles and there are some coated layers along the surface of these particles (Figure 8).

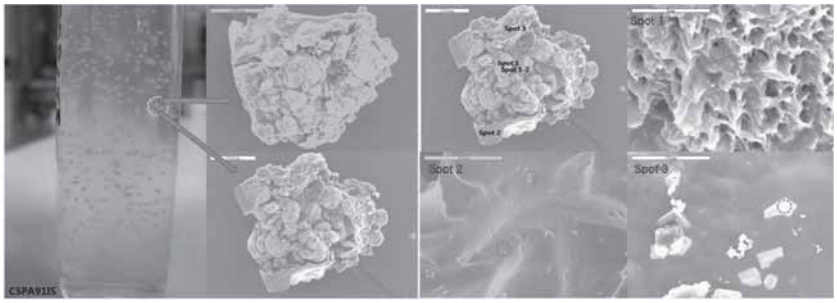

Figure 8. *Picture of C5PA91IS solution after 2 weeks storage and SEM micrographs of its by-product, white particles dispersed in the solution.*

Table 2. *EDS Results for White Unknown Particles Dispersed in Clay Composite Solution.*

	Spot 1		Spot 1-2		Spot 2		Spot 3	
Element	**Elmt %**	**Atom %**	**Elmt %**	**Atom %**	**Elmt %**	**Atom %**	**Elmt %**	**Atom %**
C K	15.08	21.97	25.06	35.64	26.24	41.95	4.46*	8.38*
O K	47.75	52.23	36.26	38.71	11.00	13.20	12.64	17.83
Na K	2.64	2.01	1.50*	1.11*	3.57	2.98	29.81	29.25
Mg K	23.61	16.99	20.55	14.43	13.22	10.44	15.19	14.10
Si K	10.92	6.80	16.62	10.11	45.97	31.42	37.90	30.44
Total	**100.00**	**100.00**	**100.00**	**100.00**	**100.00**	**100.00**	**100.00**	**100.00**

* = < 2 Sigma

Particle sizes in acidic conditions were larger than in Isoelectric Point (IEP) conditions because there were more favorable interactions between PAA chains. Resulting particles were on the order of 400–600 μm. Energy dispersive X-ray spectroscopy (EDS) (Table 2 and Figure 8) showed that the white particle portion had greater amounts of C and O and relatively small amounts of Si atoms. Other spots on broken clay gel particles and the coating layer showed higher intensity of Si and relatively weaker peaks of C and O. Therefore, phase-separated PAA particles appeared to be aggregated and dispersed in a clay gel. There were no particles in basic conditions of PAA after 6 weeks storage. This suggests that diffusion of short PAA chains to the surface of clay platelets had occurred.

To investigate specific differences in particle spacing as functions of pH and relative amount of PAA in the composite system, three plots were obtained from WAXRD as presented in Figure 9. These results confirmed the possibility of aggregated PAA particles observed during experiments. All samples showed a similar increase in d-spacing regardless of the amount of PAA used. Red lines represent positions of peaks for pure Laponite JS powder [25]. As shown in Figure 9(a), interplanar distances for (110) and (300) planes, corresponding to peak positions of 36.5 and 62 degrees, respectively, showed some increases for all pH conditions, while the characteristic peak for Laponite JS at 47.6 degree showed much larger increase under basic conditions. Under acidic conditions, no peak for (005) plane at 27.5 degree was found. Among these three samples, having the lowest PAA contents, the largest overall increase in interplanar distances at pH 6 for all planes was observed.

The peaks for (005) plane decreased as the amount of PAA increased as presented in Figure 9(b) and 9(c). More PAA content resulted in disappearance of particle orientation regularity. In the case of acidic conditions of Figure 9(b), there was a significant increase for (100) plane from 20.4 to 16.3 degrees, which means the distance increased from 4.35 Å to 5.44 Å according to the Bragg's law. This may be explained by the fact that entangled short PAA chains inserted into platelets and enlarged the spacing. Interplanar distances of most planes showed similar increases for pH 4 and 7. Less than critical amounts of PAA had no effect on interplanar distances and subsequent microstructure of clay platelets. There was no change for (100) under acidic and IEP conditions with more PAA [Figure 9(c)] because more PAA increases possibility of forming phase-separated PAA chains resulting in aggregates that are too

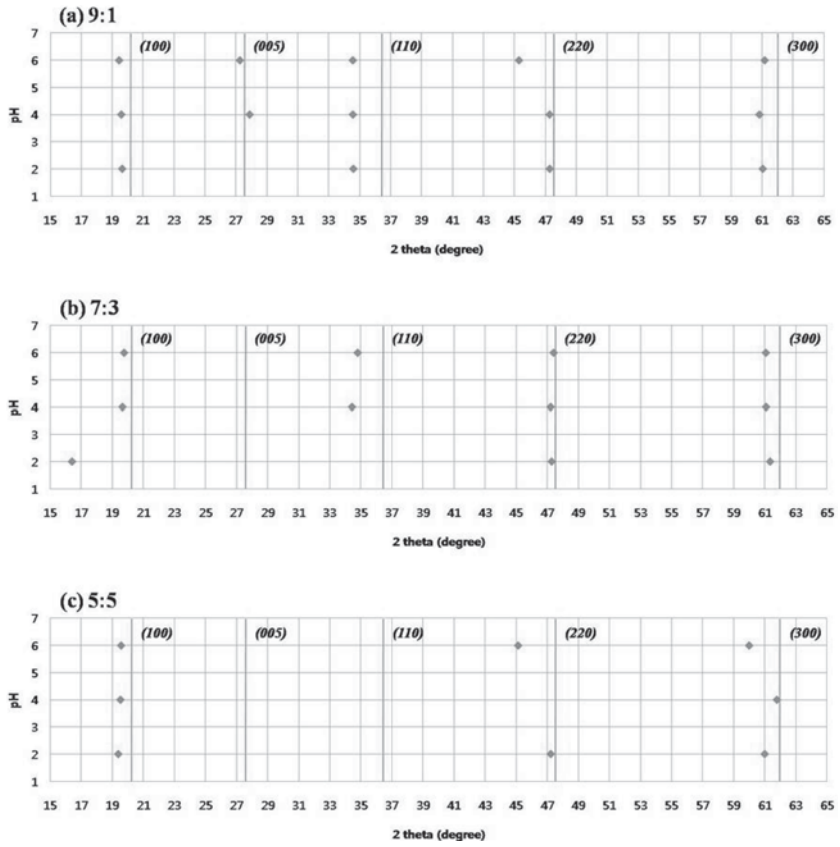

Figure 9. *Effects of the pH on the peak positions of XRD results depending on PAA content. Positions of peaks for pure Laponite JS powder are indicated.*

large to be inserted between platelets. Under basic condition, the similar tendency for increase of each interplanar spacing is shown for all PAA content except for (005) and (110) planes.

To investigate changes in position of (001) peaks depending on the amount of PAA under basic conditions, X-ray diffraction was obtained at lower angle ranges from 2 to 10 degrees (Figure 10). This figure shows that the peak observed in C5PA91BS disappeared at C5PA73BS and reappeared at C5PA55BS. This might be explained by a larger amount of oriented clay platelets in [001] direction resulting in a peak for C5PA91BS that contains more clay. However, this peak disappeared as the amount of polymer increased showing similar characteristic peaks with exfoliated samples (C5PA73BS curve of Figure 10). Finally this

peak was shifted to a lower degree possibly due to some diffusion of PAA chains into intergallery. Because of the relatively small aspect ratio compared to natural montmorilonite (MMT) or other clay types, it would be easier for the structure of Laponite JS to collapse by diffusion of polymer. Therefore, randomly collapsed structures of C5PA55BS could result in microvoids resulting in poor barrier properties.

Figure 11 shows TEM micrographs of samples prepared under basic condition (a) and acidic conditions (b) of PAA. Figure 11(a) shows that there was no apparent feature of edge-standing clay platelets or tactoids under basic conditions of PAA, while several black lines in Figure 11(b) represent edge-standing clay tactoids were separated from entangled PAA chains. Effects of shear direction on orientation of clay platelets for coating processes were shown in Figure 12. Overall intensities of C5PA91BS_c (coated layer by a coating rod) were much lower than those of C5PA91BS_p (clay composite powder) and all peaks except for (005) plane disappeared. This suggests that clay platelets were oriented in the direction that was parallel to the shear direction as illustrated in Figure 12, which conforms to the relation of shear direction with relative orientation of clay platelets reported [3,10,17]. This shows that coating

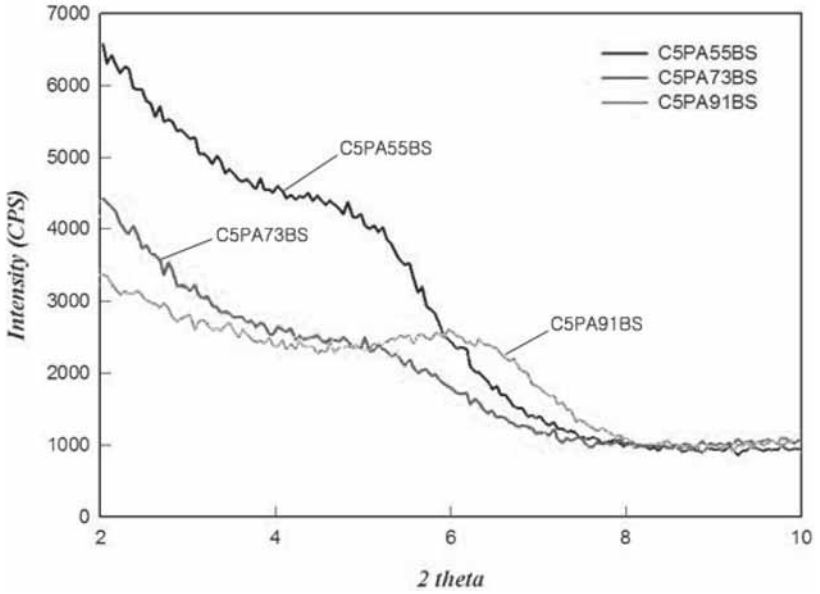

Figure 10. *Effects of the amount of PAA on the changes in basal spacing ((001) peak position) of PCN samples prepared at basic condition.*

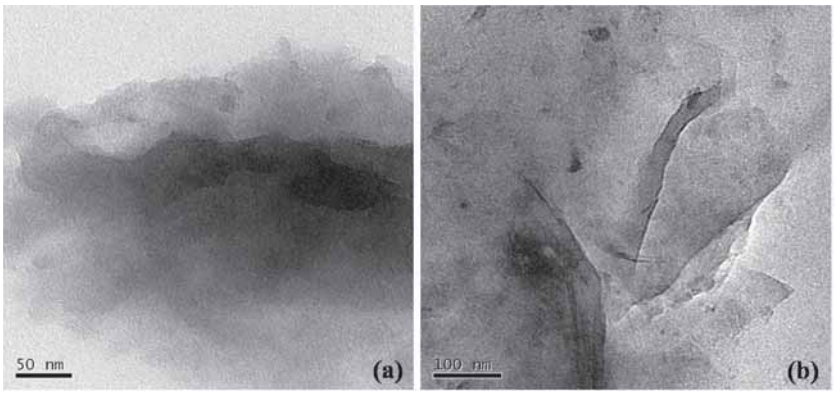

Figure 11. *TEM micrographs of C5PA73BS (a) and C5PA73AS (b).*

processes with inherent shear direction such as rod coating, doctor blade, or calendaring promise orientation of filler particles in composite systems resulting in better barrier properties.

Barrier Properties

Barrier properties of prepared composite solutions with PAAs of different pH values were investigated by measuring OTR of prepared films from each solution. From our previous work [7], it was reported that significant increases in OTR were observed for loadings in excess of 50

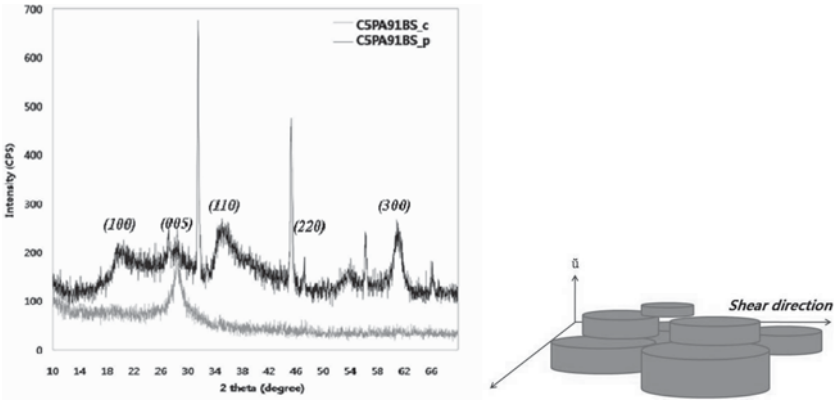

Figure 12. *XRD results of clay composite powder (C5PA91BS_p) and corresponding coated layer by a coating rod (C5PA91BS_c).*

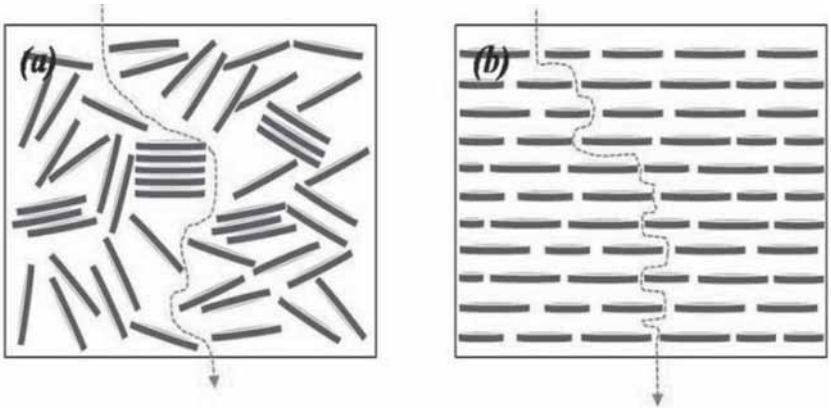

Figure 13. *Effect of clay platelet microstructure on barrier properties when the same amount of clay was arranged (a) as a randomly dispersed state and (b) as a stratified state. Red dot lines show the diffusion path of oxygen gas molecules through the PCN material.*

wt%. This is due to high degrees of reaggregation of clay as well as lower degrees of exfoliation caused by steric interference. The amount of clay in this composite system is over 50 wt% and, according to our previous results, significant decrease in barrier properties should be observed regardless of pH of polymer used. However, C5PA91BS, which contains 90 wt% of clay in the system showed good barrier properties of about 10 cc/m^2/day, which is similar with OTR of composite solution coated specimens having lower clay content with good exfoliation. This lower OTR value could be approached by densely stratified structures as shown in Figure 13. The difference in microstructure of clay platelet resulted in different barrier properties at the same amount of clay.

Figure 14 shows SEM micrographs of composite-coated i-PP surfaces. Figure 14 (a) and (b) shows small cracks in the coating surface and this lowered barrier properties of specimen dramatically by allowing gas molecules to contact to the substrate directly. The more PAA in the composite solution such as C5PA73 and C5PA55 added, the more cracks on the surface were observed, with associated high OTR values over 100 cc/m^2/day. Poor interactions between negatively charged PAA under lower pH and clay platelets likely squeezed polymer out from the microvoids and microchannel and resulted in many cracks on the coated surface [Figure 14(c) and 14(d)]. Figure 15 illustrates effects of pH on OTR, which confirm morphological features and defects of coated layers.

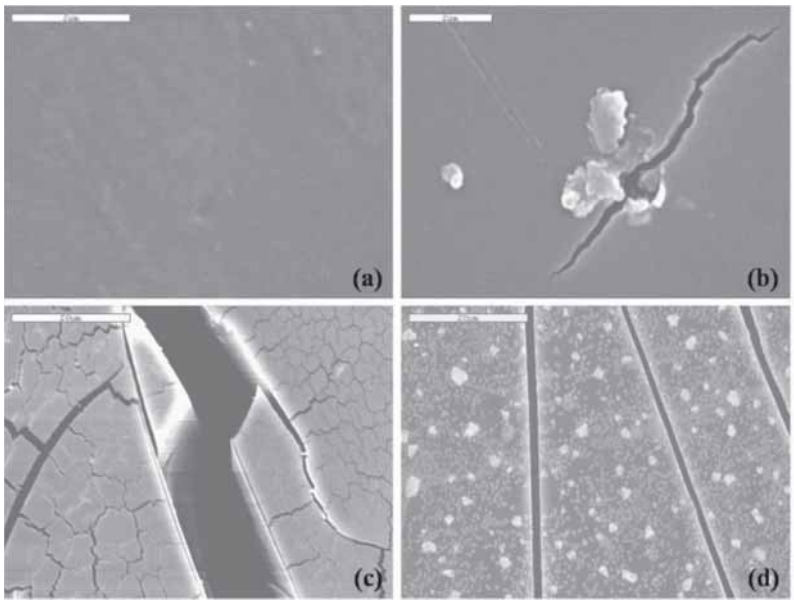

Figure 14. *SEM micrographs of nanocomposite-coated surfaces (a), (b) C5PA91BS (c) C5PA91IS (d) C5PA91AS.*

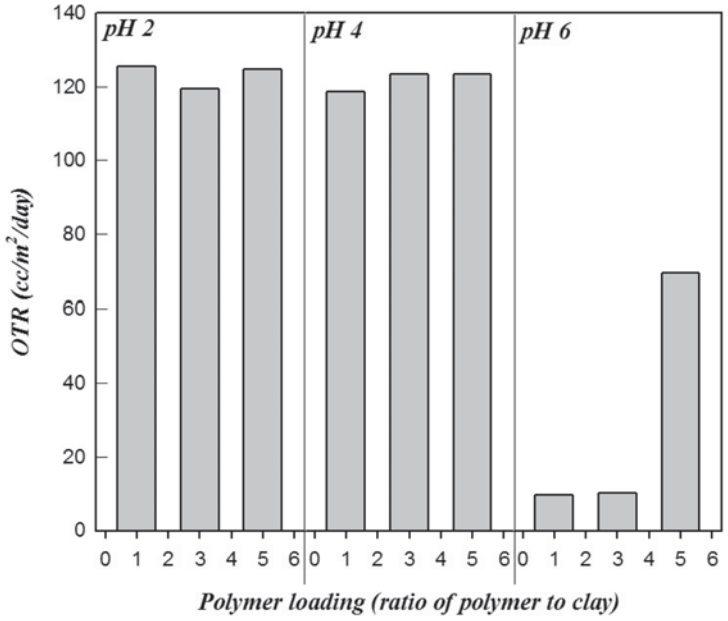

Figure 15. *Dependence of permeability on pH and the amount of PAA for highly filled PCN coating system.*

ACKNOWLEDGEMENTS

The authors would like to thank Dr. Jo Anne Ratto of the Combat Feeding Directorate, Advanced Materials Engineering Team U.S. Army Natick Soldier RD&E Center. This work was funded in part by the US Army Solid Waste Reduction Program entitled, "Nanocomposites for Optimal Packaging System" at the Natick Soldier RD&E Center Combat Feeding Directorate, Advanced Materials Engineering Team, Natick, MA.

REFERENCES

1. Osman, M.A., Mittal, V., Morbidelli, M., and Suter, U.W. (2003). Polyurethane Adhesive Nanocomposites as Gas Permeation Barrier, *Macromolecules, 36*: 9851–9858.
2. Nielsen, L.E. (1967). Models for The Permeability of Filled Polymer Systems, *J Macromol. Sci. (Chem), A1*: 929–942.
3. Malwitz, M.M., Lin-Gibson, S., Hobbie, E.K., Butler, P.D., and Schmidt, G. (2003). Orientation of Platelets in Multilayered Nanocomposite Polymer Films, *J. Polym. Sci. B: Polym. Phys., 41*: 3237–3248.
4. Picard, E., Gauthier, H., Gérard, J.-F., and Espuche, E. (2007). Influence of The Intercalated Cations on The Surface Energy of Montmorillonites: Consequences for The Morphology and Gas Barrier Properties of Polyethylene/Montmorillonites Nanocomposites, *J. Colloid and Interface Sci., 307*: 364–376.
5. Demirkol, E.A., and Kalyon, D.M. (2007). Batch and Continuous Processing of Polymer Layered Organoclay Nanocomposites, *J. Appl. Polym. Sci., 104*: 1391–1398.
6. Lee, E.C., Mielewski, D.F., and Baird, R.J. (2004). Exfoliation and Dispersion Enhancement in Polypropylene Nanocomposites by In-situ Melt Phase Ultrasonication, *Polym. Eng. And Sci., 44*: 1773–1782.
7. Kwak, J.W., Welt, B., and Beatty, C. (2009). Enhancement of Oxygen Barrier with Polymer Clay Nanocomposite Coatings on Polypropylene Treated with Atmospheric Pressure Plasma, *J Appl. Packag. Res., 3*: 39–56.
8. Lepoittevin, B., Pantoustier, N., Devalckenaere, M., Alexandre, M., Calberg, C., Jérôme, R., Henrist, C., Rulmont, A., and Dubois, P. (2003). Polymer/Layered Silicate Nanocomposites by Combinded Intercalative Polymerization and Melt Intercalation: A Masterbatch Process, *Polymer, 44*: 2033–2040.
9. Zerda, A.S., Caskey, T.C., and Lesser, A.J. (2003). Highly Concentrated, Intercalated Silicate Nanocomposites: Synthesis and Characterization, *Macromolecules, 36*: 1603–1608.
10. Koo, C.M., Kim, S.O., and Chung, I.J. (2003). Study on Morphology Evolution, Orientation Behavior, and Anisotropic Phase Formation of Highly Filled Polymer-Layered Silicate Nanocomposites, *Macromolecules, 36*: 2748–2757.
11. Okamoto, M., Nam, P.H., Maiti, P., Kotaka, T., Hasegawa, N., and Usuki, A. (2001). A House of Cards Structure in Polypropylene/Clay Nanocomposites Under Elongational Flow, *Nanoletters, 1*: 295–298.
12. Bharadwaj, R.K., Mehrabi, A.R., Hamilton, C., Trujillo, C., Murga, M., Fan, R., Chavira, A., and Thompson, A.K. (2002). Structure-Property Relationships in Cross-Linked Polyester-Clay Nanocomposites, *Polymer, 43*: 3699–3705.
13. Ebina, T., and Mizukami, F. (2007). Flexible Transparent Clay Films with Heat-Resistant and High Gas-Barrier Properties, *Adv. Mater., 19*: 2450–2453.

14. Tetsuka, H., Ebina, T., Nanjo, H., and Mizykami, F. (2007). Highly Transparent Flexible Clay Films Modified with Organic Polymer: Structural Characterization and Intercalation Properties, *J. Mater. Chem., 17*: 3545–3550.
15. Gopakumar, T.G., Lee, J.A., Kontopoulou, M., and Parent, J.S. (2002). Influence of Clay Exfoliation on The Physical Properties of Montmorilonite/Polyethylene Composites, *Polymer, 43*: 5483–5491.
16. Mongondry, P., Tassin, J.F., and Nicolai, T. (2005). Revised State Diagram of Laponite Dispersions, *J. Colloid and Interface Sci., 283*: 397–405.
17. Saunders, J.M., Goodwin, J.W., Richardson, R.M., and Vincent, B. (1999). A Small-Angle Scattering Study of The Structure of Aqueous Laponite Dispersions, *J. Phys. Chem. B, 103*: 9211–9218.
18. Bharadwaj, R.K. (2001). Modeling The Barrier Properties of Polymer-Layered Silicate Nanocomposites, *Macromolecules, 34*: 9189–9192.
19. Maiti, P., Nam, P.H., Hasegawa, M.ON., and Usuki, A. (2002). Influence of Crystallization on Intercalation, Morphology, and Mechanical Properties of Polypropylene/Clay Nanocomposites, *Macromolecules, 35*: 2042–2049.
20. Wan, W., Yu, D., Xie, Y., Guo, X., Zhou, W., and Cao, J. (2006). Effects of Nanoparticle Treatment on The Crystallization Behavior and Mechanical Properties of Polypropylene/Calcium Carbonate Nanocomposites, *J. Appl. Polym. Sci., 102*: 3480–3488.
21. Lusti, H.R., Gusev, A.A., and Guseva, O. (2004). The Influence of Platelet Disorientation on The Barrier Properties of Composites: A Numerical Study, *Modelling Simul. Mater. Sci. Eng., 12*: 1201–1207.
22. Ogoshi, T., and Chujo, Y. (2005). Synthesis of Anionic Polymer-Silica Hybrids by Controlling pH in An Aqueous Solution, *Mater. Chem., 15*: 315–322.
23. Gudeman, L.F., and Peppas, N.A. (1995). pH-Sensitive Membranes from PVA/PAA Interpenetrating Netweok, *J. of membrane sci., 107*: 239–248.
24. Cummins, H.Z. (2007). Liquid, Glass, Gel: The Phases of Colloidal Laponite, *J. Non-Crystalline Solids, 353*: 3891–3905.
25. Daniel, L.M., Frost, R.L., and Zhu, H.Y. (2008) Edge-Modification of Laponite with Dimethyl-octylmethoxysilane, *J. Colloid and Interface Sci., 321*: 302–309.

GUIDE TO AUTHORS

1. Manuscripts shall be sent electronically to the editors, Changfeng Ge at cfgmet@rit.edu and Bruce Welt at bwelt@ufl.edu using Microsoft Word in an IBM/PC format. If electronic submission is not possible, three paper copies of double-spaced manuscripts may be sent to Changfeng Ge, Editor of the *Journal of Applied Packaging Research*, Rochester Institute of Technology, One Memorial Drive, Rochester, NY 14623-5603, USA (Telephone 585-475-5391) or Bruce Welt, Editor of the *Journal of Applied Packaging Research*, University of Florida, Box 110570, Gainesville, FL 32611-0570, USA (Telephone 352-392-1864, X-111). Manuscripts should normally be limited to the space equivalent of 6,000 words. The editor may waive this requirement in special occasions. As a guideline, each page of a double-spaced manuscript contains about 300 words. Include on the title page the names, affiliations, and addresses of all the authors, and identify one author as the corresponding author. Because communication between the editor and the authors will be electronic, the email address of the corresponding author is required. Papers under review, accepted for publication, or published elsewhere in journals are normally not accepted for publication in the *Journal of Applied Packaging Research.* Papers published as proceedings of conferences are welcomed.
2. Article titles should be brief, followed by the author's name(s), affiliation, address, country, and postal code (zip) of author(s). Indicate to whom correspondence and proofs should be sent, including telephone and fax numbers and e-mail address.
3. Include a 100-word abstract and keywords.
4. If electronic art files are not supplied, submit three copies of camera-ready drawings and glossy photographs. Drawings should be uniformly sized, if possible, planned for 50% reduction. Art that is sent electronically should be saved in either a .tif or .JPEG files for superior reproduction. All illustrations of any kind must be numbered and mentioned in the text. Captions for illustrations should all be typed on a separate sheet(s) and should be understandable without reference to the text.
5. DEStech uses a numbered reference system consisting of two elements: a numbered list of all references and (in the text itself) numbers in brackets that correspond to the list. At the end of your article, please supply a numbered list of all references (books, journals, web sites etc.). References on the list should be in the form given below. In the text write the number in brackets corresponding to the reference on the list. Place the number in brackets inside the final period of the sentence cited by the reference. Here is an example [2].

   Journal: 1. Halpin, J. C., "article title", *J. Cellular Plastics,* Vol. 3, No. 2, 1997, pp. 432–435.
   Book: 2. Kececioglu, D. B. and F.-B. Sun. 2002. *Burn-In Testing: Its Quantification and Optimization,* Lancaster, PA: DEStech Publications, Inc.

6. Tables. Number consecutively and insert closest to where first mentioned in text or type on a numbered, separate page. Please use Arabic numerals and supply a heading. Column headings should be explanatory and carry units. (See example at right.)

Table 5. Comparison of state-of-the-art matrix resins with VPSP/BMI copolymers.

Resin System	Core Temp. (DSC peak)	Char Yield, %
Epoxy (MY720)	235	30
C379: H795 = 1.4	285	53

7. Units & Abbreviations. SI units should be used. English units or other equivalents should appear in parentheses if necessary.
8. Symbols. A list of symbols used and their meanings should be included.
9. Page proofs. Authors will receive page proofs by E-mail. Proof pages will be in a .PDF file, which can be read by Acrobat Reader. Corrections on proof pages should be limited to the correction of errors. Authors should print out pages that require corrections and mark the corrections on the printed pages. Pages with corrections should be returned by FAX (717-509-6100) or mail to the publisher (DEStech Publications, Inc., 439 North Duke Street, Lancaster, PA 17602, USA). If authors cannot handle proofs in a .PDF file format, please notify the editors, Changfeng Ge at cfgmet@rit.edu or Bruce Welt at bwelt@ufl.edu.
10. Index terms.With proof pages authors will receive a form for listing key words that will appear in the index. Please fill out this form with index terms and return it.
11. Copyright Information. All original journal articles are copyrighted in the name of DEStech Publications, Inc. All original articles accepted for publication must be accompanied by a signed copyright transfer agreement available from the journal editor. Previously copyrighted material used in an article can be published with the *written* permission of the copyright holder (see #14 below).
12. Headings. Your article should be structured with unnumbered headings. Normally two headings are used as follows:

    Main Subhead: DESIGN OF A MICROWAVE INSTALLATION
    Secondary Subhead: Principle of the Design Method

    If further subordination is required, please limit to no more than one (*Third Subhead*).

13. Equations. Number equations with Arabic numbers enclosed in parentheses at the right-hand margin. Type superscripts and subscripts clearly above or below the baseline, or mark them with a caret. Be sure that all symbols, letters, and numbers are distinguishable (e.g., "oh" or zero, one or lowercase "el," "vee" or Greek nu).
14. Permissions. The author of a paper is responsible for obtaining releases for the use of copyrighted figures, tables, or excerpts longer than 200 words used in his/her paper. Copyright releases are permissions to reprint previously copyrighted material. Releases must be obtained from the copyright holder, which is usually a publisher. Forms for copyright release will be sent by the editor to authors on request.

General: The *Journal of Applied Packaging Research* and DEStech Publications, Inc. are not responsible for the views expressed by individual contributors in articles published in the journal.